Journal of Science: Advanced Materials and Devices 11 (2026) 101279

Contents lists available at ScienceDirect

Journal of Science: Advanced Materials and Devices

journal homepage: www.elsevier.com/locate/jsamd

Research Article

Engineering metallic palladium-copper interfaces on titanium dioxide for efficient catalytic abatement of gaseous benzene

Kumar Vikrant [a,b,c], Myoung Won Chung [d], Seunghyun Weon [d], Danil W. Boukhvalov [e,f], Bagila Baitimbetova [f], Philippe M. Heynderickx [g,h], Ki-Hyun Kim [c,*], Eilhann E. Kwon [i,**]

[a] Center for Materials Innovation and Technology, VinUniversity, Vinhomes Ocean Park, Gia Lâm, Hanoi, 100000, Viet Nam
[b] College of Engineering and Computer Science, VinUniversity, Vinhomes Ocean Park, Gia Lâm, Hanoi, 100000, Viet Nam
[c] Department of Civil and Environmental Engineering, Hanyang University, 222 Wangsimni-Ro, Seoul, 04763, Republic of Korea
[d] School of Health and Environmental Science & Department of Health and Safety Convergence Science, Korea University, 145 Anam-Ro, Seoul, 02841, Republic of Korea
[e] College of Science, Institute of Materials Physics and Chemistry, Nanjing Forestry University, Nanjing, 210037, China
[f] Institute of Physics and Technology, Satbayev University, 11 Ibragimov Street, Almaty, 050032, Kazakhstan
[g] Center for Green Chemistry and Environmental Biotechnology (GREAT), Engineering of Materials via Catalysis and Characterization, Ghent University Global Campus, 119-5 Songdo Munhwa-ro, Yeonsu-gu, Incheon, 406-840, Republic of Korea
[h] Department of Green Chemistry and Technology, Faculty of Bioscience Engineering, Ghent University, Coupure Links 653, Ghent, B-9000, Belgium
[i] Department of Earth Resources and Environmental Engineering, Hanyang University, 222 Wangsimni-Ro, Seoul, 04763, Republic of Korea

ARTICLE INFO

Keywords:
Benzene
Copper
Catalytic oxidation
Volatile organic compounds
Palladium

ABSTRACT

The cancer-causing aromatic volatile organic compound (VOC), benzene, is a common contaminant found in the air. In this study, a reductively engineered palladium (Pd)-copper (Cu) nanoalloy supported on titanium dioxide (TiO_2) is prepared to study an exothermic pathway for the rate-limiting benzene ring-opening step *via* thermocatalytic oxidation. The catalysts are synthesized *via* wet impregnation, with controlled Pd loading followed by either oxidative (O: air calcination) or reductive (R: hydrogen (H_2) treatment at 300°C) pre-treatment. The R pre-treatment generates metallic Pd^0-Cu^0 nanoalloys on TiO_2, while the O counterpart yields isolated metal oxides. The ranking of catalytic activity for 100 ppm benzene, under experimental conditions of 250°C, gas hourly space velocity of 79,618 h^{-1}, and 0% relative humidity, is as follows: Pd/Cu-TiO_2-R (71 ± 7.9 μmol g^{-1} h^{-1}) > Cu-TiO_2-R (59 ± 0.27) > Pd/Cu-TiO_2-O (42 ± 3.4) > Cu-TiO_2-O (23 ± 0.27). The top-performing Pd/Cu-TiO_2-R catalyst also achieves the highest CO_2 yield (78.2% across 250 to 550°C). Density functional theory simulations demonstrate the mechanistic origin of this enhancement: the reductively engineered Pd-Cu nanoalloy surface provides an exothermic pathway for benzene ring-opening, whereas the oxidized surface imposes an endothermic barrier. Increased moisture (up to 60% RH) competes with benzene for active sites, reducing benzene conversion from 41.4% to 26.7%. By purposefully creating metallic Pd^0-Cu^0 interfacial sites on Pd-Cu/TiO_2 nanoalloys through a rational reductive engineering process, this research unlocks an energetically advantageous ring-opening chemical reaction, thereby forging a new design strategy for the oxidation of aromatic VOCs under mild temperature conditions.

1. Introduction

A wide array of industrial operations is responsible for the production and emission of benzene, a cancer-causing aromatic volatile organic compound (VOC) [1,2]. These sources span numerous sectors, including petroleum refining, the synthesis of organic chemicals, and the manufacturing of products like textiles, artificial leather, pharmaceuticals, pesticides, inks, adhesives, and electronics, in addition to various surface coating applications [2]. Alongside their health risks, unchecked VOC (e.g., benzene) emissions into the atmosphere are also of significant environmental concern as they contribute to the formation of ozone, secondary organic aerosols, particulate matter, and photochemical smog

* Corresponding author.
** Corresponding author.
E-mail addresses: kkim61@nate.com (K.-H. Kim), ek2148@hanyang.ac.kr (E.E. Kwon).

https://doi.org/10.1016/j.jsamd.2026.101279
Received 28 May 2026; Received in revised form 25 August 2026; Accepted 19 September 2026
Available online 5 October 2026
2468-2179/© 2026 Vietnam National University, Hanoi. Published by Elsevier B.V. This is an open access article under the CC BY license (http://creativecommons.org/licenses/by/4.0/).

[1,3,4]. For remediating industrial waste streams with high concentrations of VOCs, thermocatalytic oxidation emerges as a leading strategy, largely because it combines exceptional efficiency with a strong selectivity for producing innocuous final products, such as water (H_2O) and carbon dioxide (CO_2) [2,3]. Further, thermocatalytic oxidation is more energy-efficient in treating dilute pollutants (e.g., < 1% concentration) from various industrial streams than direct thermal combustion (requires additional fuel) [5]. As such, the former can be regarded as a more practical technology.

Metal oxide-supported noble metal (e.g., silver (Ag), gold (Au), palladium (Pd), and platinum (Pt)) catalysts (SNMCs) are the primary candidates for thermocatalytic oxidation against aromatic VOCs due to their capability to attain complete mineralization of the recalcitrant benzene ring at low temperatures with high stability even in the co-presence of other contaminants (e.g., sulfur dioxide (SO_2) and H_2O) [2,6,7]. The noble metals on the support surface offer a high capability to activate carbon-hydrogen (C-H)/carbon-oxygen (C-O) bonds in the VOC molecules while simultaneously offering heightened molecular oxygen (O_2) activation to facilitate the catalytic oxidation reaction due to their unfilled electron orbitals [8]. However, due to the exorbitant cost of SNMCs, enormous efforts have been made to explore ways to prepare cheap yet active catalysts (e.g., transition metal oxide-based catalysts (cost-effective and relatively eco-friendly) and their combinations with SNMCs) for the oxidation of benzene at relatively low temperatures [9,10]. This approach is part of a broader strategy in materials science to design synergistic nanocomposites for a wide range of environmental applications, including the photocatalytic removal of pollutants [11–14].

The noble metal content can be reduced (lowering catalyst cost) by incorporating a transition metal into the system while enhancing the catalytic activity through bimetallic synergy. For example, a cerium (Ce)-zirconium (Zr) mixed oxide (CZ)-supported copper (Cu)-Ag bimetallic catalyst (CZCuAg) attained 100% benzene (150 ppm (air balance) at 100,000 h^{-1} gas hourly space velocity (GHSV)) conversion (X_B) at 250°C (T_{100}) [15]. Copper(II) oxide (CuO) and metallic Ag (Ag^0) in CZCuAg synergistically offered adsorption/partial oxidation sites for benzene (conversion into benzoquinones) and deep oxidation sites for the intermediate benzoquinones (conversion into formate and total oxidation products), respectively, to effectively mineralize benzene in air [15]. Furthermore, adding ultralow amounts of Ag to eggshell-supported manganese dioxide (MnO_2) catalysts significantly enhanced the low-temperature oxidation activity against formaldehyde (an oxygenated VOC) due to the bimetallic synergy [16]. Consequently, utilizing low amounts of noble metals as promoters for the transition metal oxide-based catalysts could offer a practical route for utilizing SNMCs for the low-temperature VOC oxidation reactions.

The choice of Cu over other transition metals is evident from a previous result wherein the benzene oxidation activity for mesoporous silica (Santa Barbara Amorphous (SBA)-15)-supported metal oxide catalysts increased in the following order: nickel(II) oxide (NiO) < iron(II) oxide (FeO) < manganese(II) oxide (MnO) < CuO [5]. A subsequent report indicated that metallic Cu (Cu^0) generated by the high-temperature reduction of CuO/SBA-15 using hydrogen (H_2) was much more active for benzene oxidation [17]. Hence, the exact role of the Cu oxidation state in benzene oxidation remains to be addressed through a more in-depth investigation. In addition, the activity and mechanism of benzene oxidation by other noble metal-Cu systems have scarcely been explored. Furthermore, the synergistic effects in bimetallic catalysts are well-documented. However, the deliberate application of a reductive pre-treatment to engineer Pd-Cu nanoalloy interfaces for benzene oxidation remains critically underexplored. Most studies focus on synergies between metal oxides or between a noble metal and a support, often overlooking how specific pre-treatments can fundamentally alter the active sites. This work posits that creating such metallic interfaces can provide a more favorable, exothermic reaction pathway for the rate-limiting benzene ring-opening step, a hypothesis that has not been systematically investigated for Pd-Cu systems in VOC abatement.

The present work explores the thermocatalytic oxidation of benzene (~100 ppm and a GHSV of 79,618 h^{-1}) in air using Cu-titanium dioxide (TiO_2)-R, Cu-TiO_2-O, Pd/Cu-TiO_2-R, and Pd/Cu-TiO_2-O (O and R suffixes in the catalyst names indicate oxidation and reduction pre-treatments, respectively). The CO_2 yield (Y_{CO2}) has also been measured consistently to assess the benzene mineralization potential of the tested catalysts. The effects of relative humidity (RH) on benzene removal have also been explored. The specific reaction routes and governing mechanism for benzene oxidation were elucidated by linking them to the oxidation states of the metals and their surrounding electronic structure. This was accomplished using a comprehensive set of methods, including temperature-programmed analysis, thorough kinetic modeling, *in-situ* diffuse reflectance infrared Fourier transform spectroscopy (DRIFTS), thermal desorption-gas chromatography-mass spectrometry (TD-GC-MS), and density functional theory (DFT) simulation. The findings from this investigation contribute valuable new insights into how Cu and Pd species on metal oxide supports participate in benzene oxidation, which will inform the creation of practical SNMCs intended for use in actual industrial scenarios.

2. Materials and methods

2.1. Chemicals and reagents

All materials utilized in this work were acquired from commercial sources. The TiO_2 support, AEROXIDE® P25, was obtained from Evonik Industries AG, located in Essen, Germany. A separate set of reagents was provided by Sigma-Aldrich based in St. Louis, Missouri, United States of America (USA), which included palladium(II) chloride ($PdCl_2$ (≥99.9%)), copper(II) nitrate hemi(pentahydrate) ($Cu(NO_3)_2{\cdot}2.5H_2O$ (98%)), liquid benzene (≥99.9%), and silicon carbide (SiC (≥97.5%)). Furthermore, Union Gas Co., Ltd. in Yongin, South Korea, was the supplier for high-purity (99.999%) cylinders of nitrogen (N_2), H_2, and air.

2.2. Catalyst fabrication method

The fabrication of both Cu-TiO_2-O and Pd/Cu-TiO_2-O relied on a conventional wet impregnation technique [18]. The preparation of the first material, Cu-TiO_2-O, began by dissolving 3 g of $Cu(NO_3)_2.2.5H_2O$ in 20 mL of deionized (DI) H_2O with agitation (350 rpm) for 5 min at room temperature (RT). To this Cu solution, 4 g of TiO_2 was introduced, and the resulting suspension was stirred continuously for an additional 180 min under the same conditions. This mixture then underwent a two-step thermal process: first, it was dried in a convection oven at 85°C for 70 h to produce a solid cake, which was then ground into a powder. Second, this powder was calcined in a muffle furnace for 180 min at 500°C in a stagnant air atmosphere, yielding the catalyst designated as Cu-TiO_2-O. The bimetallic Pd/Cu-TiO_2-O catalyst was created through a second impregnation step. A suspension was made by dispersing 33.4 mg of $PdCl_2$ in 20 mL of DI H_2O for 5 min (350 rpm, RT). Into this Pd mixture, 2 g of the previously synthesized Cu-TiO_2-O powder was incorporated and stirred for 180 min. The subsequent drying and calcination treatments for this material were identical to the protocol described above. A final reduction treatment was applied to both materials. The Cu-TiO_2-O and Pd/Cu-TiO_2-O samples were heated in a tube furnace (Hantech Co., Ltd., Gunpo, South Korea) to 300°C (at a ramp rate of 10°C min^{-1}) and held for 60 min. This was performed under a 50 mL min^{-1} flowing gas stream of 10 vol% H_2 with N_2 as the balance. This process yielded the final catalysts, labeled Cu-TiO_2-R and Pd/Cu--TiO_2-R, respectively. An array of physicochemical techniques was employed to analyze the properties of all synthesized materials, and a comprehensive description of these methods is located in the supporting information (SI).

2.3. Catalytic performance evaluation

All catalytic tests for benzene oxidation were performed under atmospheric pressure within a fixed-bed quartz tube reactor, which had an outer diameter of 0.3 cm, an inner diameter of 0.2 cm, and a length of 17 cm. The operational temperature for these evaluations was varied between 250 and 550°C. Precise regulation of the reactor temperature was achieved through the use of an electric tube heater (Model TC200P [K], from Misung Scientific Co., Ltd., Yangju, South Korea) that was integrated with a heating block. To immobilize the catalyst bed, which consisted of a physical blend of the catalyst and SiC diluent, plugs of quartz wool sourced from the Ohio Valley Specialty Company (Marietta, Ohio, USA) were positioned within the reactor. The preparation of the gaseous working standard (G-WS) involved introducing 20 μL of liquid benzene *via* a liquid syringe (Trajan Scientific and Medical, Ringwood, Australia) into a 50 L polyester aluminum (PEA) bag pre-filled with air to create a target concentration of roughly 100 ppm. To guarantee both the total evaporation of the liquid and the achievement of equilibrium with the internal surfaces of the bag, the container was allowed to rest at RT for a duration of approximately 20 h. In line with previous experiments conducted under comparable parameters [19], an assumption was made that approximately 90% of the injected liquid benzene successfully transitioned into the gaseous phase. For tests requiring humid conditions, a VOC G-WS with approximately 60% RH was prepared by introducing 680 μL of DI H_2O into the 50 L air-filled PEA bag concurrently with the liquid benzene.

A continuous flow system was established by linking the reactor inlet to the PEA bag containing the benzene G-WS. Downstream, the reactor outlet was connected to a minipump (MP-Σ30NII, Sibata Scientific Technology, Ltd., Saitama, Japan) which drew the reactant gas through the catalyst bed at a constant rate of 50 mL min^{-1}, resulting in a GHSV of 79,618 h^{-1}. A sampling port for analysis was installed in the line between the reactor exit and this pump. Before data collection at any given temperature, the system was allowed to stabilize by maintaining the benzene G-WS flow for a minimum of 60 min to ensure steady-state conditions were reached. The quantification of both unreacted benzene and the CO_2 produced from VOC mineralization was performed concurrently using a GC from Agilent Technologies, Inc. (7890A, Santa Clara, California, USA). This instrument was equipped with a J&W DB-1 column (model number: 123-1065), a methanizer, and a flame ionization detector (FID). For each analysis, a 500 μL gas sample was manually introduced into the GC with a gastight syringe (Trajan Scientific and Medical, Ringwood, Australia). Key performance indicators such as X_B, Y_{CO2}, and the steady-state reaction rate (r) were determined using Equations (1)–(3). The calculation forr was specifically applied under differential conditions, where X_B was less than 20%. In these equations, the variables are defined as follows: the terms $C_{B,i}$ and $C_{B,o}$ correspond to the inlet and outlet benzene concentrations, $C_{CO2,o}$ is the outlet concentration of CO_2, F_B denotes the molar flow rate of benzene, and W represents the catalyst mass.

An important consideration regarding the analytical method is that the GC system employed was not configured to resolve different carbon oxide (CO_x) species. Consequently, for the purpose of calculating Y_{CO2}, the entire CO_x peak observed in the chromatogram was attributed to CO_2. This simplification is supported by two key factors. First, all oxidation experiments were conducted in an O_2-rich environment (21 vol%), which favors complete combustion. Second, corroborating evidence from the *in-situ* DRIFTS analysis, detailed later in Section 3.4.1, revealed no detectable signals corresponding to carbon monoxide (CO) during the reaction. To probe the reaction mechanism, the pathway for benzene oxidation was investigated experimentally through the use of *in-situ* DRIFTS. This analysis was performed using a Nicolet™ iS50 FTIR spectrometer (Thermo Fisher Scientific, Waltham, Massachusetts, USA) equipped with a Praying Mantis™ diffuse reflectance cell (Harrick Scientific Products Inc., Pleasantville, New York, USA). For these specific measurements, a G-WS containing 300 ppm of benzene was prepared. The experimental procedure involved loading the catalyst into the diffuse reflectance cell and performing a preliminary purge with air for 30 min. Following this pre-treatment, the *in-situ* DRIFTS spectra were collected at a constant temperature of 350°C while the catalyst was subjected to a 50 mL min^{-1} flow of the benzene G-WS.

The identification of volatile by-products resulting from benzene oxidation was accomplished *via* TD-GC-MS, following a protocol detailed in our prior work [20,21]. The experimental setup required specific pre-treatment for both the catalyst and the sampling medium. Before use, the multi-bed Carbopack™ sampling tube, which contained 50 mg each of Carbopack™ C, B, and X, underwent a thermal conditioning process under N_2 flow at 350°C for 120 min. Concurrently, the 12 mg catalyst bed was pre-conditioned inside the reactor with N_2 at 150°C for approximately 135 min. Following these preparatory steps, the oxidation reaction was initiated. A 50 ppm benzene stream was passed over the catalyst at 150°C for a duration of 60 min, with the gas flow rate held constant at 50 mL min^{-1}. During this period, all volatile species in the reactor effluent, including by-products and unreacted benzene, were trapped on the Carbopack™ tube. Subsequent analysis of the sample-loaded tube was performed on an integrated system consisting of a TD unit (Unity 2™ from Markes International Ltd., Bridgend, Wales, United Kingdom) connected to a GC-MS instrument (QP2010 Ultra from Shimadzu Corp., Kyoto, Japan). The desorbed compounds were separated using a CP-Wax column (60 m length, 0.25 mm inner diameter, 0.25 μm film thickness). The GC oven followed a specific temperature program: an initial 10 min hold at 40°C, a temperature ramp of 6°C min^{-1} up to 220°C, and a final 20 min isothermal period at 220°C. The mass spectrometer was operated in scan mode, with its ion source temperature set to 230°C.

The r does not depend on the benzene oxidation products, i.e., CO_2 and H_2O, under differential conditions ($X_B < 20\%$) [22,23]. Consequently, the empirical benzene oxidation kinetic expression can be described using Equation (4). Equation (5) can then be obtained by taking the natural logarithm of Equation (4). Ln A, α ln p_B, and β ln p_{O2} can be assumed constant under differential conditions ($X_B < 20\%$) as minor changes occur in the reactant feed gas. Hence, Equation (5) can be simplified as Equation (6). The activation energy (E_a) can thus be obtained using the slope of the linear fit between ln r and T^{-1}. A, R, T, p_B, p_{O2}, α, and β denote the pre-exponential factor, the universal gas constant, reaction temperature, benzene partial pressure, O_2 partial pressure, reaction order concerning benzene, and reaction order concerning O_2, respectively.

$$X_B(\%) = \frac{C_{B,i} - C_{B,o}}{C_{B,i}} \times 100 \tag{1}$$

$$Y_{CO_2}(\%) = \frac{C_{CO_{2,o}}}{6 \cdot C_{B,i}} \times 100 \tag{2}$$

$$r\left(\mu mol\, g^{-1}\, h^{-1}\right) = \frac{X_B \cdot F_B\ \left(\mu mol\, h^{-1}\right)}{W\ (g)} \tag{3}$$

$$r = A e^{\frac{-E_a}{RT}} p_B^{\alpha} p_{O_2}^{\beta} \tag{4}$$

$$ln\, r = ln\, A + \alpha\, ln\, p_B + \beta\, ln\, p_{O_2} - \frac{E_a}{RT} \tag{5}$$

$$ln\, r = -\frac{E_a}{RT} + C \tag{6}$$

2.4. Temperature-programmed techniques

The reducibility of the catalysts (Cu-TiO_2-O, Pd/Cu-TiO_2-O, Cu-TiO_2-R, and Pd/Cu-TiO_2-R) was investigated using H_2-temperature-programmed reduction (TPR) on an AutoChem™ II instrument from Micromeritics. Before the main analysis, each sample (50.3 ± 0.2 mg)

underwent a rigorous, multi-stage pre-treatment. This procedure began with a complete oxidation step using a 50 mL min^{-1} flow of 5% O_2 in argon (Ar). The material was then heated at 10 K min^{-1} from RT to 383.2 K and held at this temperature for 30 min to eliminate any adsorbed contaminants like moisture. Following this, the sample was cooled to 303.2 K under a 50 mL min^{-1} flow of Ar to purge any weakly bound oxygen. For the subsequent TPR measurement, the pre-treated sample was heated to 773.2 K at a constant rate of 10 K min^{-1} while exposed to a 50 mL min^{-1} (2.04 mmol min^{-1}) gas stream of 10% H_2 in Ar. To isolate the H_2 consumption signal, a cold trap maintained at −80°C with isopropyl alcohol was placed at the reactor outlet, preventing H_2O produced during the reduction from interfering with the thermal conductivity detector (TCD). An observation from these experiments was that H_2 uptake ceased for all materials at temperatures exceeding 548.2 K. To validate the experimental design, the resolution criterion for multistep reduction events, as proposed by Malet and Caballero [24] and shown in Equation (7), was applied. The terms within this equation, P, β, S_0, and $F.C_0$, correspond to the criterion limit (typically 20 K), the heating rate (K min^{-1}), the quantity of reducible species (mol), and the H_2 molar flow rate (mol min^{-1}), respectively.

$$P > \frac{\beta S_0}{FC_0} \tag{7}$$

Analysis of the experimental TPR data revealed the quantities of removable oxygen for each material. Based on the $H_2 + O^* \rightarrow H_2O + *$ stoichiometric relationship, the quantified oxygen loss from Cu-TiO_2-O, Pd/Cu-TiO_2-O, Cu-TiO_2-R, and Pd/Cu-TiO_2-R was 200.1 ± 1.4, 87.7 ± 0.6, 97.9 ± 0.7, and 35.3 ± 0.1 μmol_{O^*}, respectively. These measurements translate to available oxygen concentrations of 3.96 ± 0.11, 1.75 ± 0.04, 1.95 ± 0.04, and 0.70 ± 0.01 mol O kg_{cat}^{-1} for the same set of catalysts. To confirm that the collected TPR data possessed adequate resolution for subsequent modeling, the criterion from Malet and Caballero [24] was applied. The calculation based on Equation (7), utilizing the highest measured reducible species amount ($S_0 = 200.1$ μmol_{O^*}), the heating rate ($\beta = 10$ K min^{-1}), and the molar flow rate ($F.C_0 = 200$ μmol min^{-1}), yielded a maximum value of 9.79 K. This result is well below the typical threshold of P = 20 K, affirming the suitability of the data. The O_2-temperature-programmed desorption (TPD) profiles were acquired using the AutoChem™ II instrument. A standardized sample preparation was conducted before analysis, beginning with loading 240.6 ± 0.3 mg of the material. This sample first underwent a cleaning step where it was heated to 383.2 K at 10 K min^{-1} under a 50 mL min^{-1} helium (He) flow and held for 30 min to desorb contaminants. After cooling the cleaned sample to 298.2 K, it was saturated with oxygen by exposure to a 5% O_2 in He gas stream for 1 h. A subsequent 10 min purge with pure He at 50 mL min^{-1} was performed to eliminate any physisorbed O_2. The TPD measurement was then initiated by heating the sample to 773 K at a ramp rate of 15 K min^{-1} under a 50 mL min^{-1} He flow, with the observation that all oxygen desorption ceased before the temperature reached 598.2 K. Further information regarding the H_2-TPR model, standard deviation calculations, and TPD data analysis is available in the SI.

2.5. Computational simulation approach

To elucidate the reaction pathways and the associated energy profile for the thermocatalytic ring-opening of benzene on the reduced Pd-Cu/TiO_2 nanoalloy, DFT calculations were employed. All computational simulations for this investigation were conducted using the Spanish Initiative for Electronic Simulations with Thousands of Atoms (SIESTA) program, a software package that operates on the basis of a pseudopotential framework [25]. The theoretical basis for every analysis was the Perdew-Burke-Ernzerhof generalized gradient approximation (GGA-PBE), which was implemented with both spin-polarization and van der Waals (+vdW) corrections to ensure an accurate treatment of weak non-covalent interactions [26–28]. The complete optimization of all atomic coordinates was achieved by representing the ion cores with non-relativistic, norm-conserving pseudopotentials. For this purpose, specific cut-off radii were defined for each element: 2.30 au for Pd, 2.15 au for Cu, 2.42 au for titanium, 1.14 au for carbon, and 1.25 au for both hydrogen and oxygen [29]. Additionally, two distinct basis sets of localized orbitals were employed for the wave function expansion: a double-ζ basis was applied specifically to hydrogen atoms, while a more comprehensive double-ζ plus polarization basis was used for all other elements in the system. The energy barriers have been calculated by screening of the energy landscape.

3. Results and discussion

3.1. Characterization of synthesized materials

Analysis *via* powder X-ray diffraction (PXRD) confirmed that the characteristic crystal structure of TiO_2 P25 was present in all four catalysts prepared for this investigation [30] (Fig. 1 (a)). The anatase crystal structure was identified by a series of key diffraction signals observed at 2θ values of 48.3, 55.2, 25.3, 62.9, 38.7, 70.4, 54.1, 75.3, and 68.9°, which were assigned to the (200), (211), (101), (204), (004), (220), (105), (215), and (116) Miller indices, respectively [31] (Fig. 1 (a)). Similarly, the characteristic peaks at 27.4, 35.9, and 41.3° indicated the rutile Miller indices of (110), (101), and (111), respectively [31] (Fig. 1 (a)). The oxidation/reduction pre-treatments or Cu/Pd impregnation did not affect the TiO_2 P25 crystal structure, as evidenced by the similar PXRD patterns between all tested samples (Fig. 1 (a)). The absence of the characteristic diffraction peaks of Pd and Cu in the PXRD patterns should indirectly suggest a low amount and high dispersion of those species on the catalyst surfaces [32] (Fig. 1 (a)). All the tested catalysts exhibited excellent thermal stability under airflow in the range of RT to 800°C with insignificant mass losses of 1.5, 1.8, 1.3, and 2.2%, respectively (Fig. S1 (a)).

The mesoporous nature of all four prepared materials was confirmed by N_2 adsorption-desorption analysis, which yielded type-IV isotherms for each sample in accordance with the International Union of Pure and Applied Chemistry (IUPAC) classification system [33] (Fig. S1 (b)). A minor hysteresis loop, characteristic of the type-H3 classification [33], was observed in the N_2 adsorption-desorption isotherms for all the catalysts (Fig. S1 (b)). The Brunauer-Emmett-Teller (BET) surface areas for Cu-TiO_2-O (31 ± 0.07 m^2 g^{-1}) and Cu-TiO_2-R (30 ± 0.08 m^2 g^{-1}) were nearly identical. However, the addition of Pd resulted in a significant decrease, with the Pd/Cu-TiO_2-O and Pd/Cu-TiO_2-R materials showing values of only 19 ± 0.06 and 22 ± 0.19 m^2 g^{-1}, respectively (Table S1). This trend was also reflected in the pore structure. The pore volumes measured for Pd/Cu-TiO_2-R, Cu-TiO_2-R, Pd/Cu-TiO_2-O, and Cu-TiO_2-O were 0.031, 0.046, 0.024, and 0.047 cm^3 g^{-1}, respectively. Similarly, the average pore diameters for these materials were determined to be 4.4, 5.1, 4.3, and 5.2 nm, respectively (Table S1). An examination of the pore size distribution plots (Fig. S1 (c)) indicated that while mesopores were the dominant feature across all samples, a minor contribution from micropores in the 1.1-2 nm range was also evident. Finally, inductively coupled plasma-optical emission spectrometry (ICP-OES) was used to quantify the elemental composition. This analysis showed Cu/Pd weight percentages of 21.3/0.92 for Pd/Cu-TiO_2-R, 20.2/1.04 for Pd/Cu--TiO_2-O, 19.1/0 for Cu-TiO_2-R, and 18.8/0 for Cu-TiO_2-O (Table S1).

The Raman spectra of the tested catalysts displayed characteristic anatase peaks at 142 (E_g), 198 (E_g), 397 (B_{1g}), 520 ($B_{1g} + A_{1g}$), and 637 (E_g) cm^{-1} [32,34] (Fig. S1 (d)). The B_{1g}, A_{1g}, and E_g modes were reported to be associated with the O-Ti-O bending, antisymmetric stretching, and symmetric stretching vibrations, respectively [34]. Note that the TiO_2 P25 Raman spectrum typically matches that of the anatase phase, as the characteristic peaks for the rutile phase are often low in intensity and not easily discernible [35]. The oxidation/reduction pre-treatments or Cu/Pd impregnation did not affect the TiO_2 P25 crystal structure, as evidenced by the similar Raman spectra between

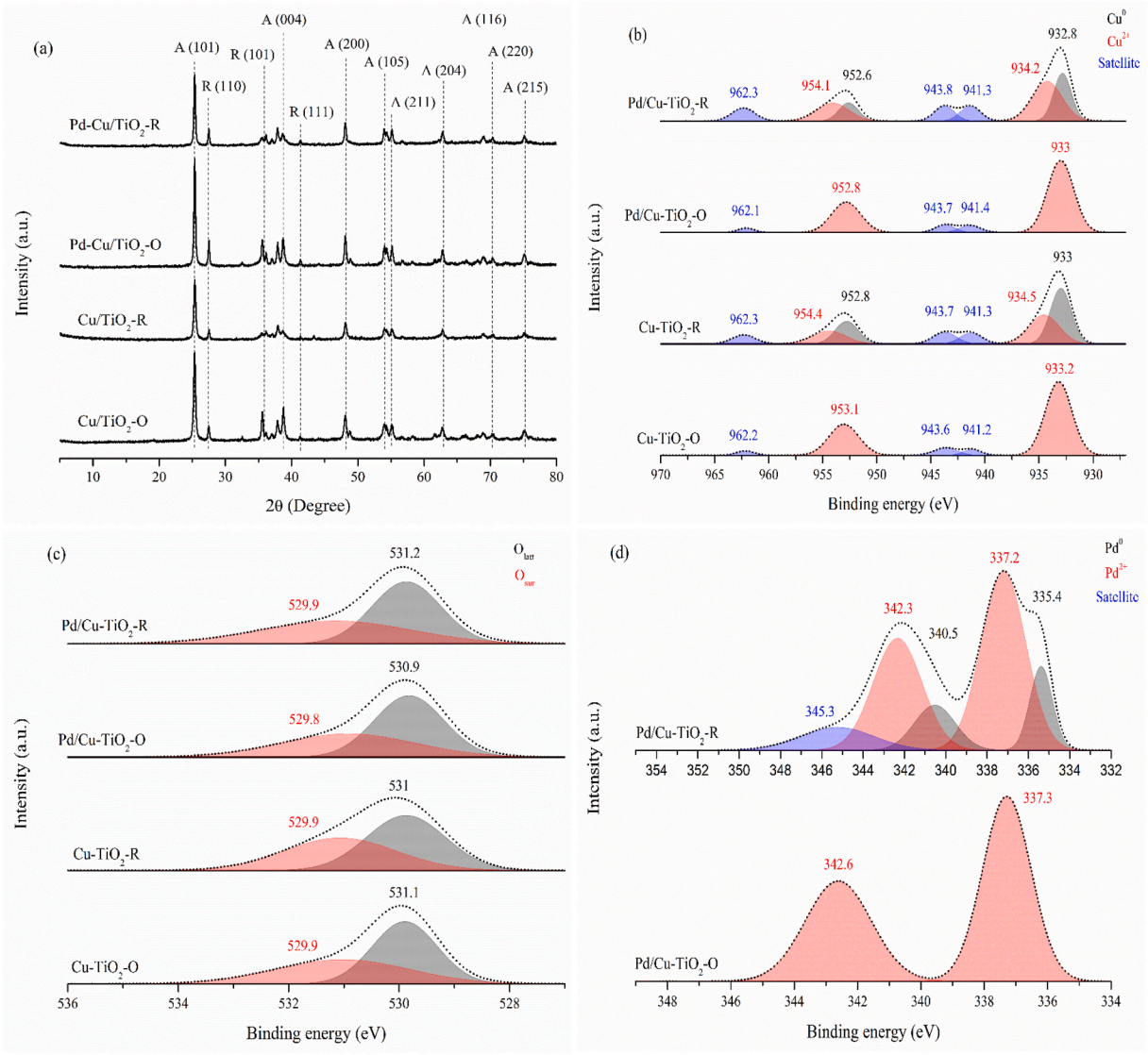

Fig. 1. Physicochemical properties of the tested catalysts. Panel (a) PXRD patterns. Panel (b) Deconvoluted Cu 2p XPS spectra. Panel (c) Deconvoluted O 1s XPS spectra. Panel (d) Deconvoluted Pd 3d XPS spectra.

samples, in line with the PXRD results (Fig. S1 (d)). The intensities of some Raman spectra peaks for the tested catalysts were low, possibly due to metal-support interactions. Following a deconvolution procedure, the Ti 2p X-ray photoelectron spectroscopy (XPS) spectra for each catalyst were resolved into three distinct components: a satellite feature observed between 458.8 and 459 eV, and a primary spin-orbit doublet consisting of the $2p_{1/2}$ state at 464.4-464.6 eV and the $2p_{3/2}$ state at 472.1-472.3 eV [30] (Fig. S2). Across all the catalysts, the binding energies (BEs) of the constituent peaks derived from the deconvoluted Ti 2p spectra exhibited negligible shifts (Fig. S2).

The Cu-TiO_2-O Cu 2p XPS spectrum could be deconvoluted into $2p_{3/2}$ (933.2 eV), $2p_{1/2}$ (953.1 eV), and three satellite peaks (941.2, 943.6, and 962.2 eV) [36] (Fig. 1 (b)). The three satellite peaks (occurring due to the shake-up process, i.e., excitation of excess electrons to higher energy states) were also observed in the deconvoluted Pd/Cu-TiO_2-R, Cu-TiO_2-R, and Pd/Cu-TiO_2-O Cu 2p XPS spectra without significant changes in the respective BEs compared to Cu-TiO_2-O [36] (Fig. 1 (b)). The characteristic Cu^0 peaks were observed in the deconvoluted Cu-TiO_2-R and Pd/Cu-TiO_2-R Cu 2p spectra at 933/952.8 and 932.8/952.6 eV, respectively (Fig. 1 (b)). The Cu^0/Cu^{2+} ratio for Pd/Cu-TiO_2-R and Cu-TiO_2-R was 0.66 and 1.3, respectively (Table S1). The lower Cu^0/Cu^{2+} ratio of the latter could stem from the fact that some amount of H_2 would have been consumed to generate metallic Pd (Pd^0), which was absent in the former. A clear indicator of the strong metal-support interaction (SMSI) resulting from the reduction pre-treatment was the shift to higher BE observed for the Cu^{2+} peak. Specifically, this peak increased by approximately +1.2 to +1.3 eV in both the Cu-TiO_2-R and Pd/Cu-TiO_2-R samples when contrasted with their oxidized precursors [34] (Fig. 1 (b)). Furthermore, the Pd-Cu interaction was evident from the redshift (decrease in BE) of ~ −0.2/0.3 in the Cu^{2+} peak position for Cu-TiO_2-O and Cu-TiO_2-R upon the addition of Pd in the system [34,37] (Fig. 1 (b)).

The O 1s spectra of all the tested catalysts could be deconvoluted into the lattice (O_{latt} (530.9-531.2 eV)) and surface oxygen (O_{sur} (529.8-529.9 eV)) peaks (Fig. 1 (c)). The $O_{sur}/(O_{sur} + O_{latt})$ ratio for the tested catalysts was similar in the 0.42-0.46 range (Table S1). The characteristic spin-orbit doublet peaks ($3d_{5/2}$ and $3d_{3/2}$) could be observed in the Pd/Cu-TiO_2-O Pd 3d XPS spectrum at 337.3 and 342.6, respectively, representing the Pd^{2+} species [38] (Fig. 1 (d)). In contrast, the Pd/Cu-TiO_2-R Pd 3d XPS spectrum could be deconvoluted into five peaks (two peaks for Pd^0, two peaks for Pd^{2+}, and a satellite peak) similar to those reported earlier for Pd-Cu/TiO_2 nanotubes (TNT) and Pd-Cu/TiO_2 nanowires (TNW) [34] (Fig. 1 (d)). The Pd^0/Pd^{2+} ratio for Pd/Cu-TiO_2-R was 0.28 (Fig. 1 (d)).

The *in-situ* CO DRIFTS data revealed that, upon reduction, the Cu-TiO_2 catalyst underwent significant changes: the disappearance of the Cu^{2+}–CO band at approximately 2175 cm^{-1} and the decline of the Cu^{+}–CO band at around 2108 cm^{-1} demonstrated that the Cu^{2+} species had been reduced, while the new shoulder (2139 cm^{-1}) indicated the formation of a distinct Cu^{+} environment, likely influenced by support interactions (Fig. S3). In the case of the Pd/Cu-TiO_2 samples, a pronounced band near 2100 cm^{-1}, which was attributed to CO adsorbed on Cu^0, became evident, suggesting an enhanced reduction process potentially aided by hydrogen spillover from Pd (Fig. S3). Moreover, the overall decrease in Cu-related CO band intensity upon Pd loading implied that Pd had partially covered the Cu sites, thereby reducing the available surface area for CO adsorption (Fig. S3).

In the high-angle annular dark-field scanning transmission electron microscopy (HAADF-STEM) images of Pd/Cu-TiO_2-O, Cu nanoparticles (NPs) were not clearly observed (Figs. S4 and S5). This could be due to the presence of Cu in its oxide form, making it difficult to identify distinct NP regions. Consequently, rather than using energy-dispersive X-ray spectroscopy (EDX) analysis to determine whether Cu and Pd coexist within specific particles, we focused on assessing the overall distribution of Cu and Pd across the sample. In contrast, the Pd/Cu-TiO_2-R images revealed metallic particles, and EDX mapping was performed on those where Cu and Pd were likely to coexist (Figs. S6–S9). Given that Cu is loaded at ~20 wt% and Pd at ~1 wt%, many particles contained only Cu. However, at a scale of approximately 10 nm, some particles containing both Cu and Pd exhibited an alloy-like structure, aligning with previous reports on Pd-Cu nanoalloys [32,39].

A cohesive structural model of the active Pd/Cu-TiO_2-R catalyst emerges from the combination of these characterization techniques. The absence of crystalline Pd or Cu peaks in the PXRD patterns (Fig. 1 (a)) indicates that the metallic species are highly dispersed or exist as very small nanoparticles (<4-5 nm detection limit). This is consistent with the HAADF-STEM images, which reveal metallic particles on the order of approximately 10 nm (Figs. S6–S9). Crucially, the EDX mapping confirms the co-localization of Pd and Cu within these individual nanoparticles, providing direct evidence for the formation of a Pd-Cu nanoalloy structure. This is further corroborated by XPS results (Fig. 1 (b)), which show a BE shift in the Cu^{2+} peak upon Pd addition, indicating a strong electronic interaction between the two metals. Taken together, this multi-faceted analysis provides strong evidence for the formation of highly dispersed Pd-Cu nanoalloy interfaces on the TiO_2 support, which are the basis for the DFT simulations and the subsequent discussion of catalytic activity.

3.2. Catalytic activity and kinetics

The benzene oxidation activity of all the catalysts tested in the present study was assessed in terms of X_B, r at 250°C, Y_{CO2}, and T_{10} and T_{50} (temperatures required to attain 10 and 50% X_B, respectively), as presented in Table 1. The X_B computed in the range of 250 to 550°C decreased in the following order: Pd/Cu-TiO_2-R (10.3 ± 1.1 – $97 \pm 0.9\%$) > Cu-TiO_2-R (8.6 ± 0 – $91.8 \pm 0.2\%$) > Pd/Cu-TiO_2-O (6.2 ± 0.5 – $86.7 \pm 3.2\%$) > Cu-TiO_2-O (3.4 ± 0 – $82.3 \pm 2.7\%$) (Fig. 2 (a)). In contrast, the Y_{CO2} computed in the range of 250 to 550°C decreased in the following order: Pd/Cu-TiO_2-R (4.4 ± 0 – $78.2 \pm 0.1\%$) > Pd/Cu-TiO_2-O (2.9 ± 1.4 – $77.6 \pm 2.1\%$) > Cu-TiO_2-R (2.4 ± 0.2 – $70 \pm 2.8\%$) > Cu-TiO_2-O (2.2 ± 0 – $61.6 \pm 3.5\%$) (Fig. 2 (b)). The T_{10}/T_{50} values increased in the following order: Pd/Cu-TiO_2-R ($249 \pm 2/317 \pm 1$°C) < Cu-TiO_2-R ($253 \pm 0/356 \pm 2.1$°C) < Pd/Cu-TiO_2-O ($264 \pm 3/389 \pm 5.5$°C) < Cu-TiO_2-O ($276 \pm 1.6/404 \pm 5.6$°C) (Table 1). The r at 250°C decreased in the following order: Pd/Cu-TiO_2-R (71 ± 7.9 μmol g^{-1} h^{-1}) > Cu-TiO_2-R (59 ± 0.27 μmol g^{-1} h^{-1}) > Pd/Cu-TiO_2-O (42 ± 3.4 μmol g^{-1} h^{-1}) > Cu-TiO_2-O (23 ± 0.27 μmol g^{-1} h^{-1}) (Table 1). The above results consistently indicate Pd/Cu-TiO_2-R as the best performer. At the same time, the benzene mineralization and oxidation increased with reduction pre-treatment, Pd loading, and reaction temperature.

The E_a for Pd/Cu-TiO_2-R was estimated as 50.9 ± 4.0 kJ mol^{-1} (Fig. S10). Furthermore, moisture negatively affected the benzene removal performance as the X_B for Pd/Cu-TiO_2-R decreased from 41.4 ± 2.3 to $26.7 \pm 3.7\%$ when the RH increased from 0 to 60% during a 4 h time-on-stream run (Fig. 2 (c)). The observed decline in benzene removal efficiency when H_2O is present can be attributed to competitive adsorption, a process where H_2O molecules and the aromatic VOC contend for the same active surface sites. Additionally, the intrinsic stability of Pd/Cu-TiO_2-R was further assessed under dry conditions (0% RH). The catalyst maintained its benzene removal activity without degradation throughout the entire 24-h time-on-stream evaluation (Fig. 2 (d)). While this long-term test confirms the inherent robustness of the catalyst, the shorter-term humid test (Fig. 2 (c)) showed that performance is impacted by competitive H_2O adsorption. A comprehensive long-term stability study under humid conditions is therefore a critical next step for assessing its industrial viability. The X_B, Y_{CO2}, and r of Pd/Cu-TiO_2-R were maintained (24 h time-on-stream) at 10.1 ± 0.2, 4.7 ± 0.2, and 70 ± 1.2 μmol g^{-1} h^{-1}, respectively, to support its high stability for the benzene oxidation reaction (Fig. 2 (d)). The consistent PXRD patterns of Pd/Cu-TiO_2-R between before and after the benzene oxidation reaction indicate that the crystal structure remained intact (Fig. S11). The catalyst exhibited remarkable durability, successfully retaining its structural integrity throughout the operational conditions of the experiment.

The benzene oxidation kinetics for Pd/Cu-TiO_2-R was modeled using four Langmuir-Hinshelwood (LH1, LH2, LH3, and LH4), four Eley-Rideal (ER1, ER2, ER3, and ER4), and three Mars-van Krevelen (MvK1, MvK2, and MvK3) models as the typical equations to describe the gas-phase oxidation kinetics for various VOCs [40,41] (Table 2). The r derived using Equation (3) was transformed from a per-mass to a per-volume basis using the bulk particle density (ρ_p (496 kg m^{-3})). Note that k_s, $K_{Benzene}$, K_{O2}, $k_{Benzene}$, k_{O2}, K_{H2O}, K_{CO2}, $p_{Benzene}$, p_{O2}, p_{H2O}, and p_{CO2} represent the rate constant for the surface reaction, the adsorption equilibrium constant for benzene, adsorption equilibrium constant for O_2, the rate constant for benzene oxidation, rate constant for catalyst reoxidation, adsorption equilibrium constant for H_2O, adsorption equilibrium constant for CO_2, benzene partial pressure, O_2 partial pressure, H_2O partial pressure, and CO_2 partial pressure, respectively. A non-linear regression analysis was employed to derive the kinetic parameters. The objective of this method was to minimize the sum of the squared errors (SSE or σ^2), which quantifies the discrepancy between the experimentally measured reaction rates (r_e) and the values calculated by the kinetic model (r_c) (Equation (8)). The coefficient of determination (R^2) (Equation (9)) and chi-squared (χ^2) (Equation (10)) values were determined to evaluate the best-fitting kinetic model to explain benzene oxidation on the Pd/Cu-TiO_2-R surface. For the purpose of this calculation, the term r_m is defined as the average value of the experimental rates (r_e).

$$SSE\ (\sigma^2) = \sum (r_e - r_c)^2 \tag{8}$$

$$R^2 = 1 - \frac{\sum (r_e - r_c)^2}{\sum (r_e - r_m)^2} \tag{9}$$

Table 1
Benzene oxidation performance of the tested catalysts.[a]

Order	Catalyst	T_{10} (°C)	T_{50} (°C)	r (μmol g^{-1} h^{-1}) at 250°C
1	Cu-TiO_2-O	276 ± 1.6	404 ± 5.6	23 ± 0.27
2	Cu-TiO_2-R	253 ± 0	356 ± 2.1	59 ± 0.27
3	Pd/Cu-TiO_2-O	264 ± 3	389 ± 5.5	42 ± 3.4
4	Pd/Cu-TiO_2-R	249 ± 2	317 ± 1	71 ± 7.9

[a] Benzene: ~100 ppm in air and flow rate: 50 mL min^{-1} (GHSV: 79,618 h^{-1}).

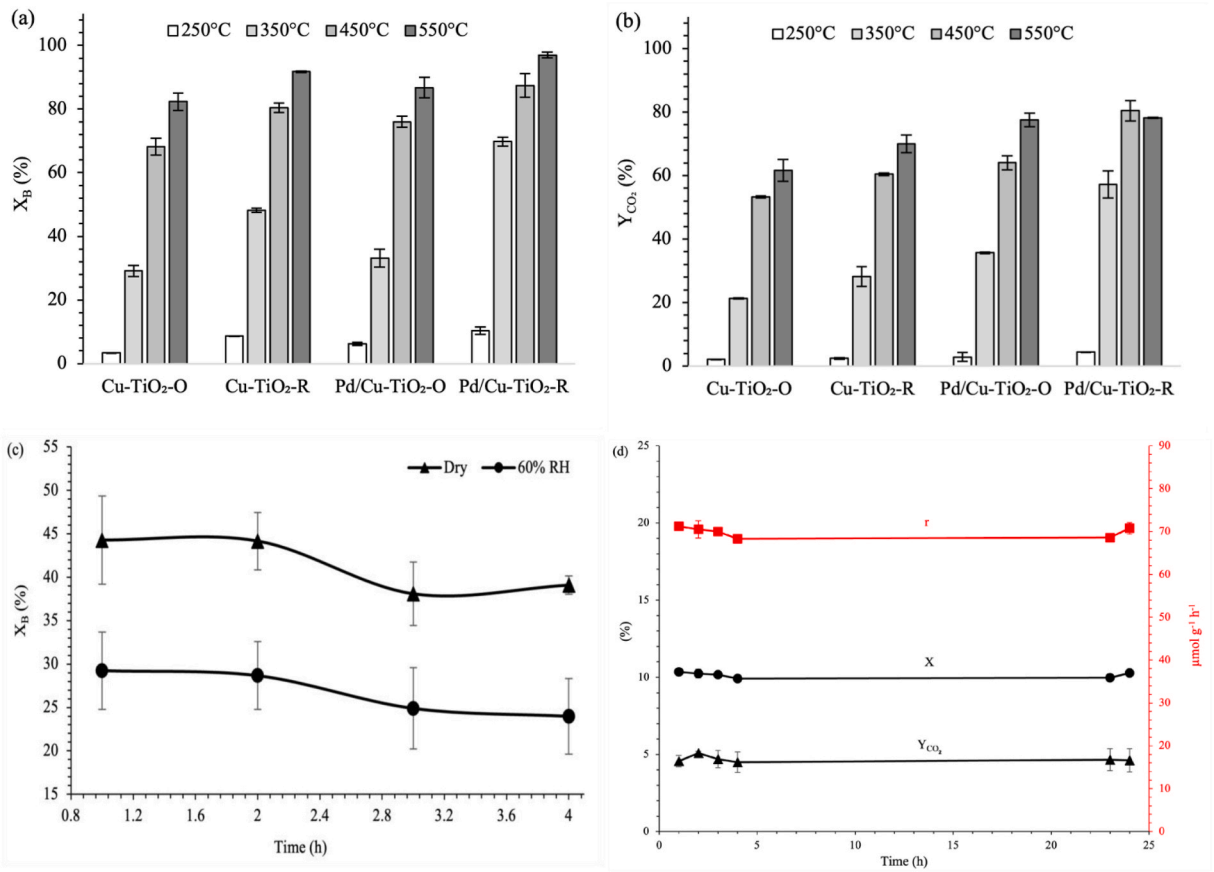

Fig. 2. Benzene oxidation performance of the tested catalysts. Panel (a) X_B versus reaction temperature (benzene: ~100 ppm in air, flow rate: 50 mL min^{-1} (GHSV: 79,618 h^{-1}), and RH: 0%). Panel (b) Y_{CO2} versus reaction temperature (benzene: ~100 ppm in air, flow rate: 50 mL min^{-1} (GHSV: 79,618 h^{-1}), and RH: 0%). Panel (c) X_B versus time-on-stream under dry and humid conditions (catalyst: Pd/Cu-TiO_2-R, benzene: ~1000 ppm in air, flow rate: 50 mL min^{-1} (GHSV: 79,618 h^{-1}), and temperature: 350°C). Panel (d) Time-on-stream stability test (catalyst: Pd/Cu-TiO_2-R, benzene: ~100 ppm in air, flow rate: 50 mL min^{-1} (GHSV: 79,618 h^{-1}), RH: 0%, and temperature: 250°C).

$$\chi^2 = \sum \frac{(r_e - r_c)^2}{r_c} \tag{10}$$

The r increased steadily from 0.008 ± 0.001 to 0.015 ± 0.001 μmol cm^{-3} s^{-1} as the $p_{Benzene}$ increased from 4.93 to 14.8 Pa (Fig. 3 (a)). Similarly, the r increased from 0.0037 ± 0.001 to 0.0065 ± 0.001 μmol cm^{-3} s^{-1} as the p_{O2} increased from 1 to 15 kPa (Fig. 3 (b)). The r displayed a sub-linear relationship with $p_{Benzene}$ (reaction order of 0.62 ± 0.02) (Fig. 3 (c)) and p_{O2} (reaction order of 0.21 ± 0.08) (Fig. 3 (d)). The r decreased steadily from 0.0066 ± 0.0010 to 0.0015 ± 0.0002 μmol cm^{-3} s^{-1} as the p_{H2O} increased from 0.63 to 2.5 kPa (Fig. 3 (e)). Similarly, the r decreased from 0.0076 ± 0.00003 to 0.007 ± 0.00002 μmol cm^{-3} s^{-1} as the p_{CO2} increased from 0.03 to 0.12 kPa (Fig. 3 (f)). The kinetic modeling results indicated that benzene oxidation on the Pd/Cu-TiO_2-R surface proceeds through the LH3 mechanism ($k_s = 0.23 \pm 0.02$ μmol cm^{-3} s^{-1}, $K_{Benzene} = 0.04 \pm 0.01$ Pa^{-1}, $K_{O2} = 0.014 \pm 0.006$ kPa^{-1}, $K_{H2O} = 0.40 \pm 0.03$ kPa^{-1}, and $K_{CO2} = 0.46 \pm 0.10$ kPa^{-1}) (Table 2). The LH R^2 values ranged from 0.896 (LH2) to 0.9615 (LH3) (Table 2). The lowest χ^2 value (1.5E-03) for the LH3 model also indicates its superiority in describing the benzene oxidation kinetics on the Pd/Cu-TiO_2-R surface (Table 2). In contrast, the χ^2 and R^2 values were significantly higher and lower, respectively, for the MvK and ER models than the LH models, indicating their incompetence in describing benzene oxidation on the Pd/Cu-TiO_2-R surface (Table 2).

3.3. H_2-TPR and O_2-TPD results

The experimental TPR data was analyzed through a modeling approach based on Equation S(1), which was used to estimate significant parameters for each catalyst. The deconvolution of these profiles, presented in Fig. 4, resolved the reduction behavior into a specific number of peaks: five were identified for the Cu-TiO_2-O, Pd/Cu-TiO_2-O, and Cu-TiO_2-R materials, while only four were needed to fit the profile for the Pd/Cu-TiO_2-R catalyst. A key distinction emerged from this analysis regarding surface reducibility. The Pd/Cu-TiO_2-R catalyst demonstrated a remarkably high efficiency, with all of its available O_{sur} being consumed at a low temperature of approximately 125°C. In contrast, the other materials required significantly higher temperatures, reaching up to 225°C, to achieve complete surface reduction. This enhanced, low-temperature reducibility of Pd/Cu-TiO_2-R provides strong evidence that supports its superior catalytic performance. The robustness of this modeling approach was validated by assessing its accuracy. The maximal average error (e_{max}), determined by comparing the model to the experimental data, was exceptionally low, peaking at just 0.47% for the Pd/Cu-TiO_2-O sample. The specific methodology for calculating this error is detailed in Equation (11). This calculation utilizes the term S, which is defined in Equation S(2) and incorporates both the total number of data points (n) and the maximum signal intensity (y_{max}) for each individual TPR experiment.

$$e_{max} = \frac{1}{y_{max}} \cdot \sqrt{\frac{S}{n}} \tag{11}$$

Table 2
Benzene oxidation kinetic models and fitting results for Pd/Cu-TiO_2-R (Note that $\gamma = 1 + K_{H2O}p_{H2O} + K_{CO2}p_{CO2}$).

Order	Model	Equation	Model assumption	Kinetic parameters	R^2	χ^2
1	LH1	$r = k_s \cdot \frac{K_{O_2} K_{Benzene} p_{O_2} p_{Benzene}}{\left(1 + K_{O_2}p_{O_2} + K_{Benzene}p_{Benzene} + K_{H_2O}p_{H_2O} + K_{CO_2}p_{CO_2}\right)^2}$	O_2 chemisorption. Involvement of one O_2 (including H_2O and CO_2).	$k_s = 0.14 \pm 0.03$ μmol cm^{-3} s^{-1}, $K_{Benzene} = 0.06 \pm 0.01$ Pa^{-1}, $K_{O2} = 0.07 \pm 0.002$ kPa^{-1}, $K_{H2O} = 0.61 \pm 0.08$ kPa^{-1}, and $K_{CO2} = 0.49 \pm 0.04$ kPa^{-1}	0.928	5.1E-03
2	LH2	$r = k_s \cdot \frac{K_{O_2}^2 K_{Benzene} p_{O_2}^2 p_{Benzene}}{\left(1 + K_{O_2}p_{O_2} + K_{Benzene}p_{Benzene} + K_{H_2O}p_{H_2O} + K_{CO_2}p_{CO_2}\right)^3}$	O_2 chemisorption. Involvement of two O_2 (including H_2O and CO_2).	$k_s = 0.23 \pm 0.05$ μmol cm^{-3} s^{-1}, $K_{Benzene} = 0.06 \pm 0.02$ Pa^{-1}, $K_{O2} = 0.16 \pm 0.002$ kPa^{-1}, $K_{H2O} = 0.64 \pm 0.09$ kPa^{-1}, and $K_{CO2} = 0.1 \pm 0.14$ kPa^{-1}	0.896	2.0E-02
3	LH3	$r = k_s \cdot \frac{\sqrt{K_{O_2}} K_{Benzene} \sqrt{p_{O_2}} p_{Benzene}}{\left(1 + \sqrt{K_{O_2}p_{O_2}} + K_{Benzene}p_{Benzene} + K_{H_2O}p_{H_2O} + K_{CO_2}p_{CO_2}\right)^2}$	Dissociative O_2 adsorption. Involvement of one O_2 (including H_2O and CO_2).	$k_s = 0.23 \pm 0.02$ μmol cm^{-3} s^{-1}, $K_{Benzene} = 0.04 \pm 0.01$ Pa^{-1}, $K_{O2} = 0.014 \pm 0.006$ kPa^{-1}, $K_{H2O} = 0.4 \pm 0.03$ kPa^{-1}, and $K_{CO2} = 0.46 \pm 0.1$ kPa^{-1}	0.9615	1.5E-03
4	LH4	$r = k_s \cdot \frac{K_{O2} K_{Benzene} p_{O2} p_{Benzene}}{\left(1 + \sqrt{K_{O2}p_{O2}} + K_{Benzene}p_{Benzene} + K_{H_2O}p_{H_2O} + K_{CO_2}p_{CO_2}\right)^3}$	Dissociative O_2 adsorption. Involvement of two O_2 (including H_2O and CO_2).	$k_s = 0.31 \pm 0.05$ μmol cm^{-3} s^{-1}, $K_{Benzene} = 0.04 \pm 0.01$ Pa^{-1}, $K_{O2} = 0.17 \pm 0.03$ kPa^{-1}, $K_{H2O} = 0.43 \pm 0.03$ kPa^{-1}, and $K_{CO2} = 0.1 \pm 0.13$ kPa^{-1}	0.9531	2.0E-03
5	ER1	$r = k_s \cdot \frac{K_{O2} p_{O2} p_{Benzene}}{1 + K_{O2}p_{O2} + K_{H_2O}p_{H_2O} + K_{CO_2}p_{CO_2}}$	O_2 chemisorption. Involvement of one O_2 (including H_2O and CO_2).	$k_s = 0.001 \pm 0.00002$ μmol cm^{-3} s^{-1} Pa^{-1}, $K_{O2} = 1 \pm 0.82$ kPa^{-1}, $K_{H2O} = 3.1 \pm 2.3$ kPa^{-1}, and $K_{CO2} = 0.38 \pm 0.08$ kPa^{-1}	0.7965	6.2E-03
6	ER2	$r = k_s \cdot \frac{K_O^2 2p_O^2 2p_{Benzene}}{\left(1 + K_{O2}p_{O2} + K_{H_2O}p_{H_2O} + K_{CO_2}p_{CO_2}\right)^2}$	O_2 chemisorption. Involvement of two O_2 (including H_2O and CO_2).	$k_s = 0.002 \pm 0.00009$ μmol cm^{-3} s^{-1} Pa^{-1}, $K_{O2} = 0.22 \pm 0.002$ kPa^{-1}, $K_{H2O} = 0.46 \pm 0.01$ kPa^{-1}, and $K_{CO2} = 0.49 \pm 0.004$ kPa^{-1}	0.6944	4.7E-02
7	ER3	$r = k_s \cdot \frac{\sqrt{K_{O2}p_{O2}} p_{Benzene}}{1 + \sqrt{K_{O2}p_{O2}} + K_{H_2O}p_{H_2O} + K_{CO_2}p_{CO_2}}$	Dissociative O_2 adsorption. Involvement of one O_2 (including H_2O and CO_2).	$k_s = 0.002 \pm 0.00006$ μmol cm^{-3} s^{-1} Pa^{-1}, $K_{O2} = 0.15 \pm 0.018$ kPa^{-1}, $K_{H2O} = 0.93 \pm 0.0002$ kPa^{-1}, and $K_{CO2} = 0.46 \pm 0.007$ kPa^{-1}	0.8271	4.4E-03
8	ER4	$r = k_s \cdot \frac{K_{O2} p_{O2} p_{Benzene}}{\left(1 + \sqrt{K_{O2}p_{O2}} + K_{H_2O}p_{H_2O} + K_{CO_2}p_{CO_2}\right)^2}$	Dissociative O_2 adsorption. Involvement of two O_2 (including H_2O and CO_2).	$k_s = 0.003 \pm 0.0001$ μmol cm^{-3} s^{-1} Pa^{-1}, $K_{O2} = 0.26 \pm 0.004$ kPa^{-1}, $K_{H2O} = 0.44 \pm 0.04$ kPa^{-1}, and $K_{CO2} = 0.46 \pm 0.02$ kPa^{-1}	0.7842	8.4E-03
9	MvK1	$r = \frac{k_{O2} k_{Benzene} p_{O2} p_{Benzene}}{k_{O2} p_{O2} \gamma + 7.5 k_{Benzene} p_{Benzene}}$	One oxidized site and one reduced site. H_2O and CO_2 adsorption on oxidized sites.	$k_{O2} = 0.003 \pm 0.0002$ μmol cm^{-3} s^{-1} kPa^{-1}, $k_{Benzene} = 0.06 \pm 0.02$ μmol cm^{-3} s^{-1} Pa^{-1}, $K_{H2O} = 0.48 \pm 0.01$ kPa^{-1}, and $K_{CO2} = 0.5 \pm 0.0001$ kPa^{-1}	0.0255	5.4E-02
10	MvK2	$r = \frac{k_{Benzene} p_{Benzene}}{\gamma^2} \cdot \left(\gamma + \frac{k_{Benzene} p_{Benzene}}{k_{O_2} p_{O_2}} - \sqrt{7.5\gamma \frac{k_{Benzene} p_{Benzene}}{k_{O_2} p_{O_2}} + \left(\frac{k_{Benzene} p_{Benzene}}{k_{O_2} p_{O_2}}\right)^2}\right)$	One oxidized site and two reduced sites. H_2O and CO_2 adsorption on oxidized sites.	$k_{O2} = 0.28 \pm 0.000001$ μmol cm^{-3} s^{-1} kPa^{-1}, $k_{Benzene} = 0.001 \pm 0.0001$ μmol cm^{-3} s^{-1} Pa^{-1}, $K_{H2O} = 0.4 \pm 0.000001$ kPa^{-1}, and $K_{CO2} = 0.5 \pm 0.00001$ kPa^{-1}	0.87	3.5E-03
11	MvK3	$r = \frac{k_{O_2} p_{O_2}}{7.5} \cdot \left(\frac{1}{\left(1 + \gamma \sqrt{\frac{k_{O_2} p_{O_2}}{7.5 k_{Benzene} p_{Benzene}}}\right)^2}\right)$	Two oxidized sites and two reduced sites. H_2O and CO_2 adsorption on oxidized sites.	$k_{O2} = 0.005 \pm 0.0002$ μmol cm^{-3} s^{-1} kPa^{-1}, $k_{Benzene} = 0.04 \pm 0.002$ μmol cm^{-3} s^{-1} Pa^{-1}, $K_{H2O} = 0.49 \pm 0.005$ kPa^{-1}, and $K_{CO2} = 0.51 \pm 0.00007$ kPa^{-1}	0.5081	2.9E-02

Table S2 gives the results for the O_{sur} concentration. The quantification of removed oxygen atoms from each material yielded distinct values: 35.3 ± 0.1 μmol_{O^*} from Pd/Cu-TiO_2-R, 97.9 ± 0.7 μmol_{O^*} from Cu-TiO_2-R, 87.7 ± 0.6 μmol_{O^*} from Pd/Cu-TiO_2-O, and 200.1 ± 1.4 μmol_{O^*} from Cu-TiO_2-O. The above corresponds to an O_{sur} concentration (available for H_2 reduction) of 3.96 ± 0.11, 1.75 ± 0.04, 1.95 ± 0.04, and 0.70 ± 0.01 mol_{O^*} kg_{cat}^{-1} for the used catalysts. As expected from the reduction treatment, the reduced catalysts, on average, show ~42% lower O_{sur} concentration (see Fig. S12). In other words, the available oxygen concentration on the Cu-based catalyst is reduced by a factor of 2.3 ± 0.1, whereas, for the Pd-Cu catalyst, the reduction amounts to a factor of 2.8 ± 0.1. Comparing the oxidized catalysts, the addition of Pd to Cu-TiO_2-O notably reduced its available O_{sur} by approximately a factor of two compared to Cu-TiO_2-O. The above effect was even more pronounced in the reduced (R) counterparts, where the ratio increases to about 2.5. This suggests that the presence of Pd may partially block some O_{sur} sites from reacting with H_2, although these sites might serve as adsorption sites for benzene during typical catalytic conditions. While the catalytically active sites under oxidation conditions may differ from those measured *via* H_2 reduction, the concentration of this readily reducible O_{sur} can serve as a useful proxy for comparing the intrinsic activity of the catalysts. By normalizing the reaction rates by the O_{sur} concentration, we can calculate an estimated turnover rate (in μmol $mol_{O^*}^{-1}$ s^{-1}). This provides a valuable metric for comparing the per-site activity, giving the order Pd/Cu-TiO_2-R (28.0 ± 3.13) > Cu-TiO_2-R (9.39 ± 0.20) > Pd/Cu-TiO_2-O (5.99 ± 0.50) > Cu-TiO_2-O (1.61 ± 0.05), which nicely emphasizes the superior performance of Pd/Cu-TiO_2-R in the studied benzene oxidation reaction (being ~ 3 (or 17) times more active than the second-highest (or least active) catalyst).

The proportional share that each individual H_2 consumption peak represents within the total signal is detailed in Table S3. The order of the first reduction peak temperature (with corresponding % contribution) is Cu-TiO_2-R (54.9 ± 0.6°C, 0.4%) < Pd/Cu-TiO_2-R (62.1 ± 0.3°C, 4.4%) < Pd/Cu-TiO_2-O (78.9 ± 0.2°C, 1.4%) < Cu-TiO_2-O (82.3 ± 1.9°C, 9.0%). The

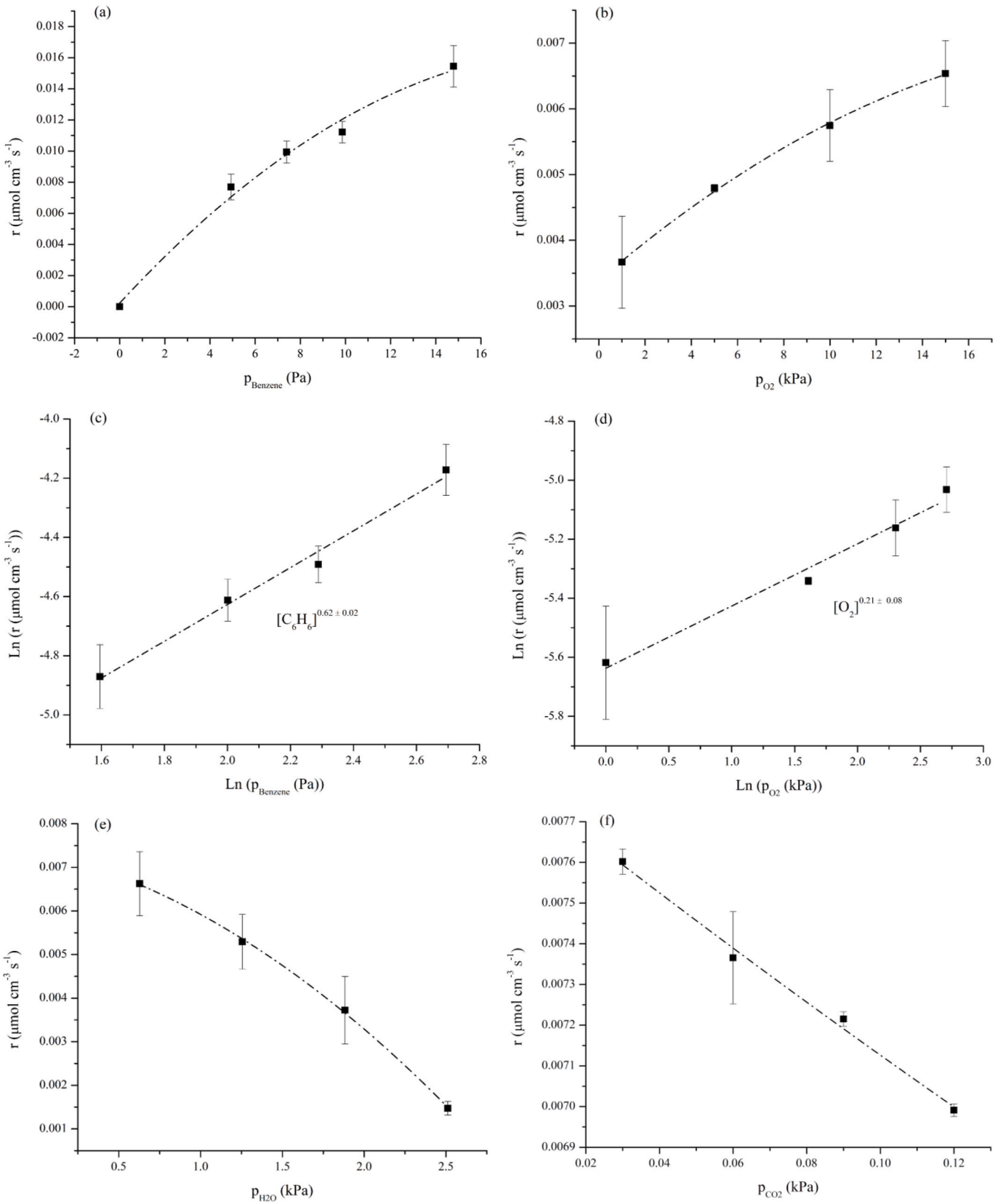

Fig. 3. Benzene oxidation kinetics for Pd/Cu-TiO_2-R (m_{cat}: 10 mg, flow rate: 50 mL min^{-1}, and temperature: 285°C). Panel (a) r as a function of $p_{Benzene}$ (p_{O2}: 21 kPa). Panel (b) r as a function of p_{O2} ($p_{Benzene}$: 4.93 Pa). Panel (c) Benzene reaction order estimation. Panel (d) O_2 reaction order estimation. Panel (e) r as a function of p_{H2O} ($p_{Benzene}$: 4.93 Pa and p_{O2}: 21 kPa). Panel (f) r as a function of p_{CO2} ($p_{Benzene}$: 4.93 Pa and p_{O2}: 21 kPa). Error bars represent standard deviation of two runs.

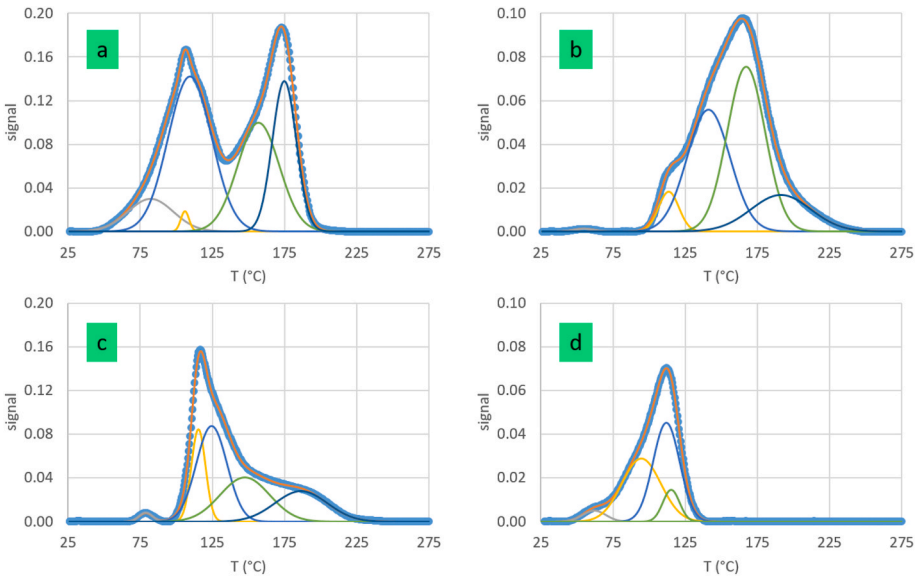

Fig. 4. H_2-TPR profiles for the used catalysts. Panel (a) Cu-TiO_2-O. Panel (b) Pd/Cu-TiO_2-O. Panel (c) Cu-TiO_2-R. Panel (d) Pd/Cu-TiO_2-R. Gaussian model, according to Equation S(1), for (—) peak 1 (—), peak 2 (—), peak 3 (—), peak 4, (—) peak 5, and (—) the total calculated signal.

apparent inconsistency where the first peak temperature of Cu-TiO_2-R is lower than that of Pd/Cu-TiO_2-R was resolved by considering the available $O_{sur.}$ The contribution of O_{sur} in the first reduction peak was ~4.4 times smaller for Cu-TiO_2-R (0.35 μmol_{O^*}) than for Pd/Cu-TiO_2-R (1.55 μmol_{O^*}), in line with the experimentally observed reactivity order. While the initial desorption peak, which occurs at the lowest temperature, accounts for only a small portion of the total signal, this specific type of O_{sur} is believed to be the primary active species in the oxidation process. This is because the O_2-rich reaction environment facilitates the continuous replenishment of these sites. This characteristic allows this oxygen to function as a readily available and quickly regenerating reservoir under typical oxidation conditions. An evaluation of the total cumulative amount of O* removed from each material established a clear performance hierarchy, as illustrated in Fig. 5 (a) and (b). The ranking determined from this data is as follows: Cu-TiO_2-O > Pd/Cu-TiO_2-R > Pd/Cu-TiO_2-O > Cu-TiO_2-R. Notably, Pd/Cu-TiO_2-R is reduced at lower temperatures than Pd/Cu-TiO_2-O, indicating that O_{sur} species on Pd/Cu-TiO_2-R are more weakly bound and therefore more readily reducible. This feature exemplifies the high catalytic activity of Pd/Cu-TiO_2-R, even with a lower absolute concentration of O_{sur}.

The O_2-TPD profiles for all catalysts are displayed in Fig. 6. A deconvolution of these profiles revealed a striking difference: while five distinct peaks were necessary to accurately model the O_2 desorption data for most of the catalysts, the profile for Cu-TiO_2-R was adequately fitted with only three peaks. The quality of these model fits was excellent, with the Pd/Cu-TiO_2-R catalyst showing a maximum average error of only 1.24%. This discrepancy in the number of peaks can be interpreted by considering the Hüttig temperature (T_H), a concept that estimates the temperature at which significant surface atom diffusion, sintering, and recrystallization begin. This temperature is calculated as $T_H = \alpha.T_m$, where α is a constant (approximately 1/3), and T_m is the bulk

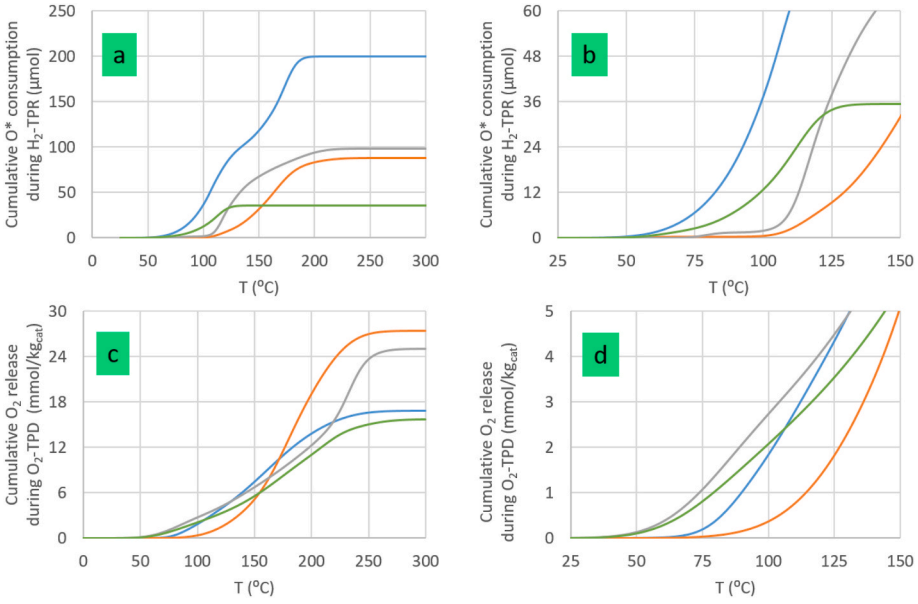

Fig. 5. H_2-TPR and O_2-TPD results for the tested catalysts. Panels (a and b) Cumulative O* consumption during H_2-TPR, Panels (c and d) cumulative O_2 release during O_2-TPD (—). Cu-TiO_2-O (—), Cu-TiO_2-R (—), Pd/Cu-TiO_2-O, and (—) Pd/Cu-TiO_2-R. Panels (b) and (d) represent a magnified part of panels (a) and (c), respectively.

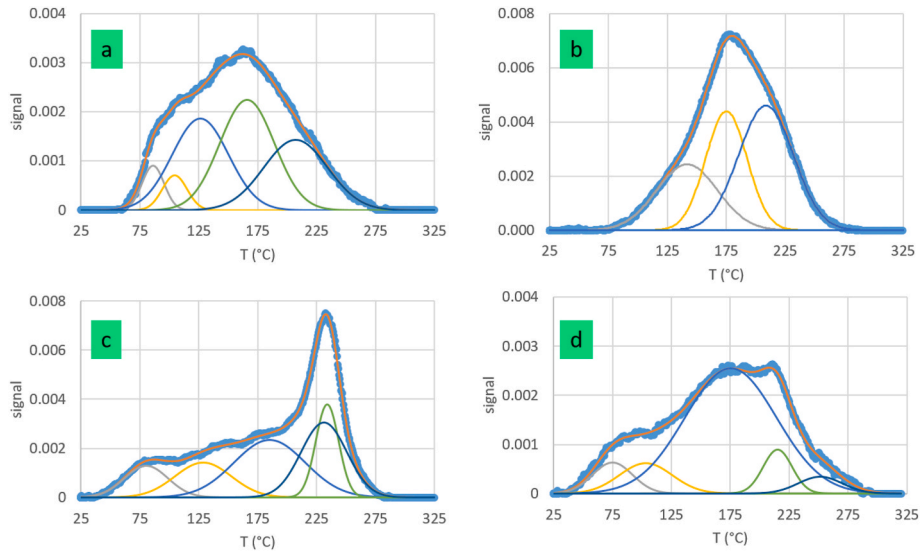

Fig. 6. O_2-TPD profiles for the tested catalysts (at a heating rate of 15 K min^{-1}). Panel (a) Cu-TiO_2-O. Panel (b) Cu-TiO_2-R. Panel (c) Pd/Cu-TiO_2-O. Panel (d) Pd/Cu-TiO_2-R. Gaussian model, according to Equation S(1), for (—) peak 1 (—), peak 2 (—), peak 3 (—), peak 4, (—) peak 5, and (—) the total calculated signal.

melting point of the material in Kelvin. Based on their respective melting points of 1358 K and 1828 K, the T_H for Cu is approximately 453 K (180°C), while for Pd it is much higher at 609 K (336°C). The catalyst synthesis involved a reduction step at 300°C. This temperature is substantially above the T_H for Cu, suggesting that this treatment likely induced Cu particle clustering. Such an agglomeration would reduce the heterogeneity of the surface, leading to fewer distinct types of oxygen adsorption sites, which aligns perfectly with the observation of only three desorption peaks. In direct contrast, the 300°C reduction temperature is well below the T_H for Pd. Consequently, Pd is expected to remain highly dispersed and stable on the support without significant clustering, explaining why both Pd-containing catalysts retained five distinct desorption peaks.

The O_2 uptake for the Cu-TiO_2-R catalyst (27.4 ± 0.4 $mmol_{O2}$ kg_{cat}^{-1}) was higher than for the unreduced Cu-TiO_2-O catalyst (16.8 ± 0.3 $mmol_{O2}$ kg_{cat}^{-1}) (Table S3). This can be explained by the creation of O_{sur} vacancies (OVs) during the reductive pretreatment. In fact, these sites are known for their higher affinity for O_2. For the Pd-based catalysts, an opposite trend was observed in O_2 uptake, with uptakes of 25.0 ± 0.4 (Pd/Cu-TiO_2-O) and 15.7 ± 0.3 (Pd/Cu-TiO_2-R) $mmol_{O2}$ kg_{cat}^{-1}. As Pd was added to the Cu-TiO_2-O catalyst during synthesis, some active sites for O_2 adsorption were likely covered to lower the concentration of surface OVs, as suggested by the H_2-TPR data presented above. The order for the O_2 desorption temperature (first peak) was Pd/Cu-TiO_2-R (74.9 ± 3.8°C, 7.6%) < Pd/Cu-TiO_2-O (80.5 ± 0.9°C, 10.7%) < Cu-TiO_2-O (86.0 ± 1.3°C, 5.5%) < Cu-TiO_2-R (141.7 ± 1.1°C, 25.5%). Although the contribution for the first desorption peak was ~2.2 times smaller on the Pd/Cu-TiO_2-R catalyst (1.19 $mmol_{O2}$ kg_{cat}^{-1}) than on the Pd/Cu-TiO_2-O catalyst (2.68 $mmol_{O2}$ kg_{cat}^{-1}), its lower desorption temperature indicates higher activity. From Fig. 5 (c) and (d), it was observed that the desorption order follows (O) > (R) for both catalyst types (Cu and Cu + Pd). The above corresponds to the higher affinity for O_2 on the reduced catalysts. Further inspection reveals that the Pd-containing catalysts exhibit the highest O_2 desorption at lower temperatures to signify that oxygen adsorbates are more rapidly desorbed or, in other words, more loosely bound, which is indicative of the overall higher activity of these Pd-containing catalysts.

3.4. Benzene oxidation mechanism and pathway

3.4.1. In-situ DRIFTS and TD-GC-MS analyses

Fig. 7 (a)-(d) display the *in-situ* DRIFTS spectra collected for the Pd/Cu-TiO_2-R, Cu-TiO_2-O, Pd/Cu-TiO_2-O, and Cu-TiO_2-R catalysts. A key finding from this analysis is that the fundamental reaction pathway for benzene oxidation remains unchanged regardless of the catalyst pretreatment (oxidation or reduction) or the inclusion of Pd. This conclusion is supported by the remarkable similarity of the spectral bands observed across all four materials. An examination of the specific intermediates reveals distinct signals for carboxylate species in two spectral regions, 1435-1437 cm^{-1} and 1552-1568 cm^{-1} [42]. Additionally, vibrational bands corresponding to acetate species were assigned to the features located between 1312 and 1324 cm^{-1} [42]. In the high-wavenumber region of 3604-3905 cm^{-1}, all catalysts exhibited characteristic bands confirming the presence of surface hydroxyl (OH) groups. These groups are formed from the dissociation of H_2O molecules, which are a final product of the complete mineralization of benzene.

In the surface OH region (3600-3900 cm^{-1}), distinct differences were observed among the catalysts during benzene oxidation. The minimal catalytic activity of the Cu-TiO_2-O material and its correspondingly weak interaction with benzene were clearly demonstrated by a unique spectral feature: a solitary, sharp band at 3648 cm^{-1}. This single peak, assigned to isolated OH species, signifies that a negligible amount of H_2O was produced, confirming that the complete mineralization of benzene barely occurred (Fig. 7 (a)). In contrast, Pd/Cu-TiO_2-R, Pd/Cu-TiO_2-O, and Cu-TiO_2-R exhibited broader and multiple OH bands over a wider wavenumber range (e.g., 3604-3905 cm^{-1}), reflecting the accumulation of surface OH species formed *via* dissociation of H_2O generated during oxidation (Fig. 7 (b)-(d)). These evolving OH signals indicate more effective benzene activation and deeper oxidation, in line with the higher catalytic performance of the reduced (R) and Pd-containing catalysts (see Section 3.2).

The absence of surface-bound aromatic intermediates such as phenolate, catecholate, and benzoquinone in the *in-situ* DRIFTS spectra suggests that benzene oxidation proceeded rapidly and irreversibly under the applied reaction conditions [43]. Instead, the identification of ring-opening products (e.g., carboxylate, acetate, and OH species) indicates that oxidation and ring-cleavage steps occur efficiently upon activation of benzene. Kinetic analysis revealed that the reaction follows the LH3 mechanism, specifically involving dissociative adsorption of O_2 (see Section 3.2). It is probable that the availability of reactive O_{sur} species enhances the rate of the oxidation process, thereby reducing the duration aromatic intermediates spend adsorbed on the catalyst surface. Taken together, the evidence from this study indicates that the kinetic

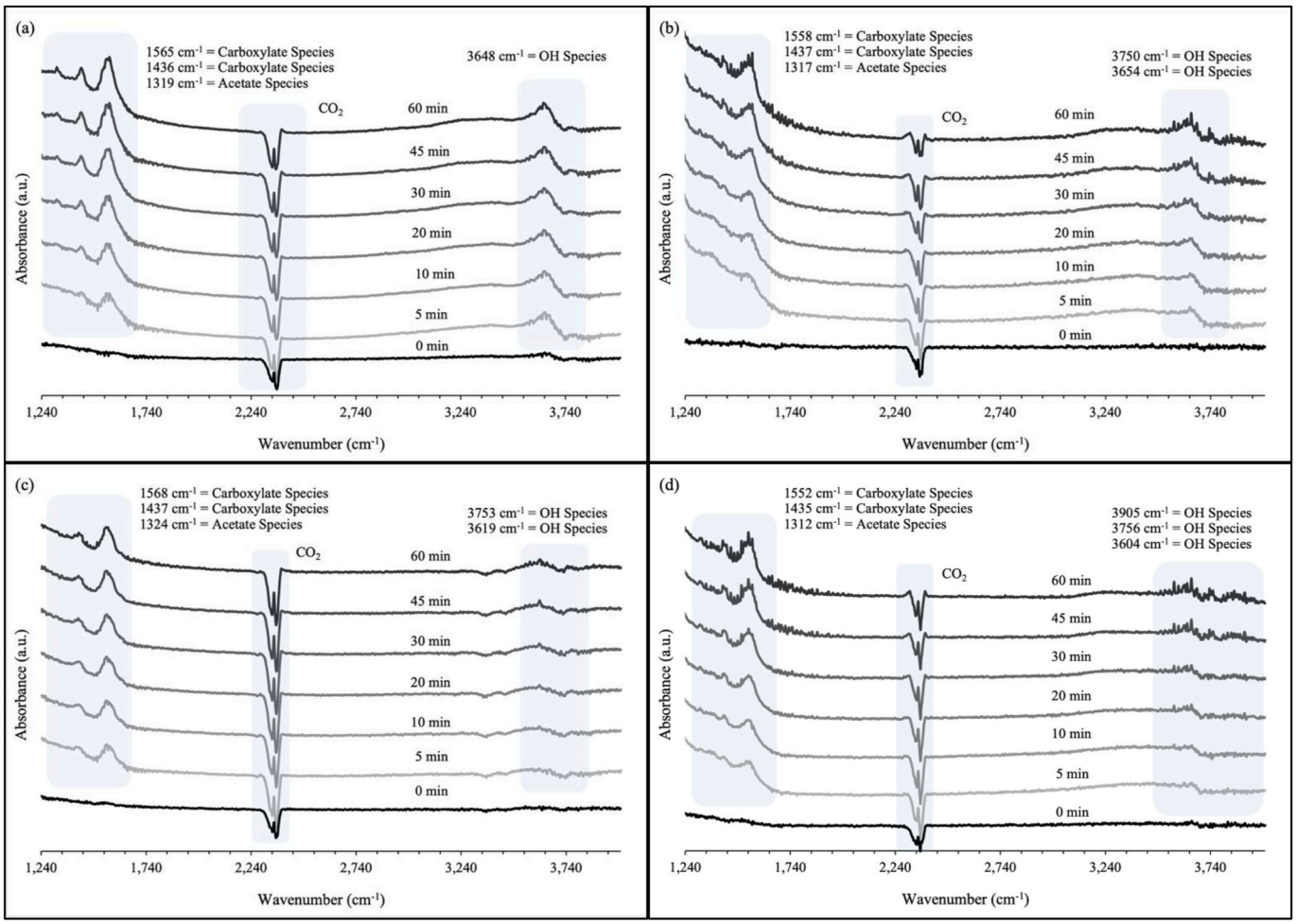

Fig. 7. *In-situ* DRIFTS spectra of the tested catalysts. Panel (a) Cu-TiO_2-O. Panel (b) Cu-TiO_2-R. Panel (c) Pd/Cu-TiO_2-O. Panel (d) Pd/Cu-TiO_2-R.

bottleneck of the reaction is not the ring-opening process or the subsequent oxidation of aromatic intermediates. Instead, the rate-limiting stage appears to be the primary interaction between benzene and the catalyst, specifically its initial surface adsorption or the activation of a C-H bond. This early-stage limitation simultaneously governs the overall reaction speed and prevents any significant buildup of observable aromatic species on the catalyst surface.

Applying TD-GC-MS to the reactor outflow identified several volatile by-products whose presence, as depicted in Fig. 8, corresponds to discrete stages within the oxidative degradation pathway of gaseous

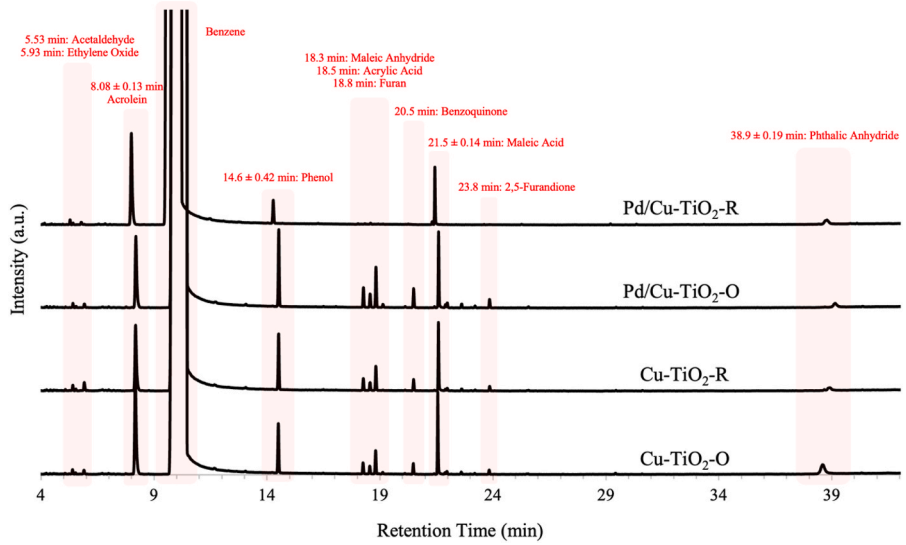

Fig. 8. TD-GC-MS chromatograms for the tested catalysts for identifying the formed volatile by-products during benzene oxidation in air.

benzene. Early-eluting compounds such as acetaldehyde (5.53 min) and ethylene oxide (5.93 min) indicated initial ring-opening events, likely through epoxide or Criegee intermediate formation [44,45]. Ethylene oxide, being highly reactive, may decompose into formaldehyde or formyl radicals, which could further react to form formic acid or participate in condensation pathways [46–48]. However, these volatile C_1-C_2 species were not detected, possibly due to the limited trapping efficiency of Carbopack™ tubes for low-molecular-weight compounds. The presence of acrolein (8.08 ± 0.13 min) as a major intermediate suggests pathways involving either butadiene oxidation (derived from benzene ring cleavage) or aldol condensation of smaller aldehydes [45,49,50]. Its presence is mechanistically critical, as acrolein serves as a precursor to furan (18.8 min) *via* cyclization or recombination reactions [51,52]. Phenol (14.6 ± 0.42 min), the dominant primary oxidation product, forms through electrophilic aromatic hydroxylation, while its subsequent oxidation yields benzoquinone (20.5 min) [15,30,43]. Parallel ring-opening of phenolic intermediates leads to maleic anhydride (18.3 min) and maleic acid (21.5 ± 0.14 min), likely *via* dienediol or muconate pathways. The detection of 2,5-furandione (23.8 min) further supports the involvement of furan derivatives in deep oxidation. In this process, furan may undergo hydroxylation or decarbonylation to form acrylic acid (18.5 min). The late-eluting phthalic anhydride (38.9 ± 0.19 min) reflects extensive degradation, likely through benzoquinone coupling or carboxylate condensation [53,54].

The observed variations in retention times (as reflected by the ± values) for some compounds (e.g., acrolein, phenol, maleic acid, and phthalic anhydride) likely stemmed from minor fluctuations in GC column temperature, carrier gas flow rate, or interactions within the complex reaction matrix. Such variability is common in GC-MS analyses of multicomponent mixtures, where competitive adsorption and slight changes in experimental conditions can influence elution times [55,56]. Despite their transient detection in the gas phase by TD-GC-MS, the absence of surface-bound phenolate or benzoquinone in the *in-situ* DRIFTS spectra indicated that these aromatic intermediates were rapidly oxidized to ring-opened products (e.g., carboxylates and acetates). This observation was further corroborated by the TD-GC-MS identification of advanced oxidative intermediates such as maleic anhydride, maleic acid, and 2,5-furandione, which arise from the subsequent fragmentation and rearrangement of these unstable aromatic species.

The by-product distribution patterns were directly correlated with the established activity trend of Cu-TiO_2-O < Cu-TiO_2-R < Pd/Cu-TiO_2-O < Pd/Cu-TiO_2-R (see Section 3.2). The Pd/Cu-TiO_2-R catalyst showed superior benzene oxidation capability with markedly fewer partial oxidation products. This enhanced performance originated from the combined effects of Pd sites activating O_2, OVs in the reduced catalyst facilitating surface redox cycles, and synergistic interactions within the Pd-Cu system that promoted deeper oxidation pathways. The persistence of high-retention-time products like phthalic anhydride and maleic acid, especially on less active catalysts, indicated their tendency toward incomplete oxidation. Conversely, the Pd/Cu-TiO_2-R catalyst demonstrated a high selectivity for the complete oxidation pathway, efficiently converting benzene into CO_2 and H_2O while simultaneously suppressing the formation of undesirable intermediate compounds.

3.4.2. DFT simulation

XPS spectra demonstrate significant oxidation of Cu and Pd, even in the reduced samples (Fig. 1 (b) and (d)). The extent of oxidation observed is too significant to be explained only by the oxidation of the metallic NPs present on the catalyst surface. Consequently, the migration of some metal atoms to the surface of TiO_2 likely occurred. According to PXRD data (Fig. 1 (a)), the anatase (101) surface is the most abundant facet in the studied materials. Thus, we simulated substitutional and interstitial Cu and Pd centers on this surface. For these simulations, we used a slab constructed from a $2 \times 4 \times 4$ TiO_2 supercell in the anatase phase. First, we optimized the atomic positions and the lattice constant of TiO_2 unit cells. The deviation from experimental values was within one percent. Hence, the chosen pseudopotentials and computational model are adequate for the planned simulations. Second, we rotate the obtained lattice constants matrix and coordinates to turn from [001] to [101] orientation and multiply the unit cell accordingly. The supercell contains 96 atoms (32 unit cells of TiO_2). To construct the slab, we introduce a vacuum layer of 4 nm within periodic boundary conditions. The thickness of the slab and the distance between identical points on the surface are more than 1 nm. The calculated formation energies show that for both species, incorporation into the (101) surface as an interstitial impurity (Fig. 9) is an exothermic process, in contrast to the formation of a substitutional defect. Hence, the latter was excluded from further consideration. XPS also reveals a decrease in the number of Cu-O and Pd-O bonds upon reduction. Therefore, to simulate the reduced samples, we created an oxygen vacancy (OV) near an interstitial impurity.

First, we simulated reactions over the Cu-TiO_2-O (oxidized) and Cu-TiO_2-R (reduced) substrates. Reducing the surface does not significantly affect the favorability of benzene and O_2 adsorption on the active sites (Fig. 9 (a) and (b)). A significant thermodynamic difference distinguishes the subsequent reaction of an adsorbed benzene molecule with an oxygen species on the two substrates. This step requires an energy input (is endothermic) on the Cu-TiO_2-O surface, but it releases energy (is exothermic) on the Cu-TiO_2-R surface. The energy barrier for this step is about 30 kJ mol^{-1}, which is about four times smaller than the energy gain. In the favorable exothermic case, the cleavage of the benzene ring is accomplished through the formation of a C-O-C bridge (Fig. 9 (b)). A release of energy characterizes the third and fourth reaction steps on both catalytic surfaces. However, on the reduced substrate, subsequent O_2 adsorption occurred without further cleavage of the benzene ring. The presence of a Pd impurity near the Cu site slightly increases the energy of benzene and O_2 physisorption (Fig. 9 (c) and (d)). In contrast to the Cu-TiO_2-O system, the second step on Pd/Cu-TiO_2-O is exothermic, with the energy barrier being about 25 kJ mol^{-1}. However, further O_2 adsorption is energetically unfavorable (the third step in Fig. 9 (c)). Conversely, on the reduced surface, all steps are exothermic (Fig. 9 (d)). The formation of OH groups during the third and fourth stages of the reaction is a significant finding that aligns qualitatively with the data obtained from the *in-situ* DRIFTS spectra (Fig. 7).

Similar to the Cu-TiO_2-R substrate, the reaction over Pd/Cu-TiO_2-R leads to the ring-opening of the benzene molecule in the early steps. However, on Pd/Cu-TiO_2-R, complete breaking of the benzene ring occurred. Therefore, the computational modeling confirms that the

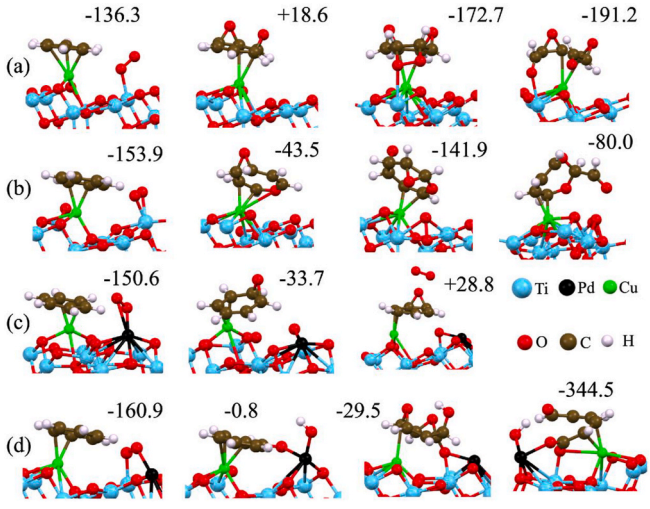

Fig. 9. Optimized atomic structures and corresponding formation energies (all in kJ mol^{-1}) for the initial steps of benzene oxidation over (a) Cu-TiO_2-O, (b) Cu-TiO_2-R, (c) Pd/Cu-TiO_2-O, and (d) Pd/Cu-TiO_2-R.

early stages of benzene oxidation on the reduced substrates are energy-releasing and proceed *via* the cleavage of the aromatic ring. The energy gains and the extent of benzene ring degradation are greater over the Cu-Pd pair. In contrast, the oxidation of benzene over unreduced samples requires overcoming at least one endothermic step. The computational outcomes therefore corroborate the performance ranking that was established through experimentation. In the real samples, various types of impurities exist; even in unreduced samples, some OVs are present, and in Pd-Cu co-doped samples, some impurities exist separately. Therefore, the improvement in catalytic performance with increasing temperature may be attributed to the activation of these less favorable reaction pathways.

3.5. Benzene oxidation performance comparison

The single-component benzene oxidation performance of the Cu-containing catalysts was compared between this work and those reported in the literature. This comparison primarily utilized r as the primary metric, given its ability to quantify the catalytic activity by accounting for major reaction variables (e.g., X_B, $C_{B,i}$, reaction temperature, volumetric flow rate, and W) (Table 3). As mentioned in Section 2.3, the r computation is only valid under differential conditions. Hence, the r values at the X_B of 10% were computed for performance comparison purposes as summarized in Table 3. In terms of the r value, Pd/Cu-TiO_2-R (70 μmol g^{-1} h^{-1}) surpassed most other reported catalysts and those prepared in this work. Exceptions include $Cu_{0.6}$manganese (Mn) (173 μmol g^{-1} h^{-1}), 7%-CuO-SBA-15 (2038 μmol g^{-1} h^{-1}), and copper cobaltite ($CuCo_2O_4$) (232 μmol g^{-1} h^{-1}) (Table 3).

In an effort to make a more accurate comparison of benzene oxidation catalytic activity, the r was normalized by BET surface area (r_{BET}) and metal loading (r_{metal}) (the latter applicable only to SNMCs) (Table 3). This approach standardizes the metric for intrinsic catalytic performance by accounting for differences in active site density and accessibility. In terms of r_{BET} (μmol m^{-2} h^{-1}), the benzene oxidation performance decreased in the following order: 7%-CuO-SBA-15 (4.04) > Pd/Cu-TiO_2-O (3.58) > Pd/Cu-TiO_2-R (3.18) > $CuCo_2O_4$ (2.46) > Cu-TiO_2-R (2.31) > Cu-TiO_2-O (2.15) > CZCuAg (0.899) > Cobalt $(Co)_{4.75}Cu_{0.25}$Aluminum (Al) (0.764) > $Cu_{0.6}$Mn (0.649) > 8%-MnO_2-2%CuO/aluminum oxide (Al_2O_3)-$Ce_{0.45}Zr_{0.45}$Yttrium $(Y)_{0.05}$Lanthanum $(La)_{0.05}O_{1.95}$ (0.398) (Table 3). In terms of r_{metal} (μmol g^{-1} h^{-1}), the benzene oxidation performance decreased in the following order: 7%-CuO-SBA-15 (36,400) > 8%-MnO_2-2%CuO/Al_2O_3-$Ce_{0.45}Zr_{0.45}Y_{0.05}La_{0.05}O_{1.95}$ (603) > Cu-TiO_2-R (364) > Cu-TiO_2-O (354) > Pd/Cu-TiO_2-O (320) > Pd/Cu-TiO_2-R (315) (Table 3). This comparison yields two key insights. First, the ranking by r_{BET} demonstrates that the Pd-promoted catalysts exhibit exceptionally high intrinsic activity per unit of surface area. Their performance outperforms most other materials reported in the literature, being surpassed only by the leading 7%-CuO-SBA-15 catalyst. Second, the shift in rankings when normalized by metal loading (r_{metal}) underscores the influence of the support material. The superior metal loading-based performance of the 7%-CuO-SBA-15 catalyst is attributed to its high-surface-area support. Nevertheless, the catalysts prepared in this work remain competitive, which confirms that Pd promotion is a successful strategy for enhancing catalytic activity.

A broader comparison further highlights the advantages of the Pd/Cu-TiO_2-R catalyst. In terms of reaction temperature, our catalyst achieves significant conversion at 250°C, which is competitive with or superior to many of the listed catalysts (Table 3). Regarding stability, the catalyst demonstrated excellent durability over a 24-h time-on-stream test (Fig. 2 (d)), a crucial parameter often missing in initial catalyst screening studies. Most importantly, from a practical standpoint, is the efficiency of noble metal usage. While the 7%-CuO-SBA-15 catalyst shows high activity, our Pd/Cu-TiO_2-R catalyst utilizes only ~1 wt% Pd. The bimetallic synergy with Cu dramatically enhances the intrinsic activity of Pd, leading to a cost-effective design where a small amount of noble metal is used to promote a much cheaper transition metal. This strategy of promoting a low-cost material represents a more economically viable path for large-scale VOC abatement compared to catalysts relying on high loadings of noble metals or expensive supports.

Finally, the apparent first-order rate constant (k_{app}) was calculated as a key performance indicator to assess the catalytic activity. It was derived under differential conditions, where low X_B ensures negligible changes in reactant concentration and temperature across the catalyst bed. Under differential conditions, the reaction rate (-r) can be modeled by a pseudo-first-order expression ($-r = k_{app}.C_{B,i}$). Consequently, k_{app}

Table 3
Performance comparison of Cu-containing catalysts reported in the literature for the thermocatalytic oxidation of single-component benzene in air.

Order	Catalyst	BET surface area (m^2 g^{-1})	Metal loading (wt.%)[a]	W (g)	T_{10} (°C)	$C_{B,i}$ (ppm)	$C_{B,i}$ (μmol mL^{-1})	Flow rate (mL h^{-1})	F_B (μmol h^{-1})	r (μmol g^{-1} h^{-1})[b]	r_{BET} (μmol m^{-2} h^{-1})[c]	r_{metal} (μmol g^{-1} h^{-1})[d]	k_{app} (mL g^{-1} h^{-1})[e]	Reference
1	8%-MnO_2-2%CuO/Al_2O_3-$Ce_{0.45}Zr_{0.45}Y_{0.05}La_{0.05}O_{1.95}$	101.7	6.7	0.1	195	700	0.018	2220	40.4	40.4	0.398	603	2220	[57]
2	$Cu_{0.6}$Mn	266	-	0.1	150	1000	0.029	6000	173	173	0.649	-	6000	[58]
3	7%-CuO-SBA-15	504	5.6	0.08	175	10,000	0.272	6000	1631	2038	4.04	36,400	7500	[17]
4	$Co_{4.75}Cu_{0.25}$Al	66.1	-	0.1	175	516	0.014	3600	50.5	50.5	0.764	-	3600	[59]
5	$CuCo_2O_4$	94	-	0.1	200	1000	0.026	9000	232	232	2.46	-	9000	[42]
6	Ce-Zr mixed oxide (CZ) CuAg	48	-	0.8	150	150	0.004	79,980	345	43	0.899	-	9998	[15]
7	Cu-TiO_2-O	31	18.8	0.01	276	100	0.002	3000	6.65	67	2.15	354	30,000	This Study
8	Cu-TiO_2-R	30	19.1	0.01	253	100	0.002	3000	6.94	69	2.31	364	30,000	This Study
9	Pd/Cu-TiO_2-O	19	21.24	0.01	264	100	0.002	3000	6.80	68	3.58	320	30,000	This Study
10	Pd/Cu-TiO_2-R	22	22.22	0.01	249	100	0.002	3000	7.00	70	3.18	315	30,000	This Study

[a] Only valid for SNMCs.
[b] Calculated by fixing the X_B at 10%.
[c] BET surface area normalized r.
[d] Metal loading normalized r.
[e] The apparent first-order rate constant (k_{app}) represents the volume of reactant processed per gram of catalyst per hour under differential conditions, standardizing activity comparisons across varying benzene concentrations.

can be defined as the r normalized by the reactant concentration. Such a normalization facilitates the direct comparison of the intrinsic catalytic activities across various materials for a given reaction, such as the gas-phase oxidation of benzene in air. In this regard, the catalysts utilized in the present work displayed a remarkably high k_{app} of ~30,000 mL g^{-1} h^{-1}, which was three times higher than the next best performer, i.e., CZCuAg (9998 mL g^{-1} h^{-1}) (Table 3). For other reported catalysts ($CuCo_2O_4$, $Co_{4.75}Cu_{0.25}Al$, 7%-CuO-SBA-15, $Cu_{0.6}Mn$, and 8%-MnO_2-2%CuO/Al_2O_3-$Ce_{0.45}Zr_{0.45}Y_{0.05}La_{0.05}O_{1.95}$), the computed k_{app} values were found to be moderately low: 9,000, 3,600, 7,500, 6,000, and 2220 mL g^{-1} h^{-1}, respectively (Table 3). The above results indicate that the catalysts from the present work surpass many comparable materials reported in the literature for the thermocatalytic oxidation of benzene in air.

4. Conclusion

This research established the exceptional catalytic activity of Pd/Cu-TiO_2-R when applied to the thermocatalytic oxidation of benzene in an air environment. Among the four catalysts tested in this work (i.e., Cu-TiO_2-O, Cu-TiO_2-R, Pd/Cu-TiO_2-O, and Pd/Cu-TiO_2-R), the reduced Pd-promoted catalyst (Pd/Cu-TiO_2-R) exhibited the highest activity, achieving a r of 71 ± 7.9 μmol g^{-1} h^{-1} at 250°C. The Y_{CO2} further confirmed the highest mineralization efficiency of 78.2 ± 0.1% at 550°C. Experimentally, it was determined that a reductive pre-treatment (H_2 at 300°C) was crucial for this high performance. Characterization *via* XPS and *in-situ* DRIFTS confirmed that this treatment generated metallic Cu^0 and Pd^0 species, forming a Pd-Cu nanoalloy interface. Kinetic analysis showed the reaction follows the LH3 mechanism, while performance tests confirmed excellent 24-h stability but also revealed a negative impact from humidity due to competitive adsorption. To elucidate the mechanistic origin of the enhanced activity, DFT calculations were performed. These theoretical simulations provided a clear distinction between the catalyst surfaces: the reductively engineered Pd^0-Cu^0 metallic interface offers an energetically favorable, exothermic pathway for the critical benzene ring-opening step. In contrast, the oxidized catalyst surface imposes an endothermic energy barrier for the same reaction. This fundamental difference, revealed by DFT, provides the core explanation for the superior performance of the reduced catalyst observed experimentally. The formation of the Pd^0-Cu^0 nanoalloy interface creates unique electronic properties that facilitate the activation of O_2, as supported by O_2-TPD results showing weaker oxygen binding on the reduced catalyst. Comparative analysis with literature catalysts showed that Pd/Cu-TiO_2-R outperformed most Cu-based systems. Its normalized rate ($r_{BET} = 3.18$ μmol m^{-2} h^{-1}) and k_{app} (30,000 mL g^{-1} h^{-1}) surpassed alternatives such as $CuCo_2O_4$ and CZCuAg. The superior activity was attributed to the Pd-Cu nanoalloy structure, which enhanced surface reactivity, as supported by HAADF-STEM analysis. The synthesis method employed - conventional wet impregnation followed by calcination and reduction - is highly scalable and widely used in industrial catalyst manufacturing, ensuring good preparation reproducibility. From an industrial feasibility perspective, the simplicity of the method and reliance on common commercial precursors (TiO_2, $Cu(NO_3)_2$, and $PdCl_2$) are significant advantages. While regeneration ability was not explicitly tested, the robust thermal stability of the catalyst up to 800°C and its consistent performance over 24 h suggest a high resistance to deactivation, which is a promising indicator for a long operational lifespan and potential for thermal regeneration. Future work should build upon the stability demonstrated here by investigating performance under more demanding scenarios, such as exposure to higher humidity levels, competitive adsorption from mixed VOC streams, and long-term activity cycling to fully assess their potential for practical applications.

CRediT authorship contribution statement

Kumar Vikrant: Writing – review & editing, Writing – original draft, Visualization, Validation, Software, Resources, Project administration, Methodology, Investigation, Funding acquisition, Formal analysis, Data curation, Conceptualization. **Myoung Won Chung:** Writing – review & editing, Writing – original draft, Visualization, Validation, Methodology, Investigation, Formal analysis, Data curation. **Seunghyun Weon:** Writing – review & editing, Writing – original draft, Visualization, Validation, Software, Resources, Project administration, Methodology, Investigation, Formal analysis, Data curation. **Danil W. Boukhvalov:** Writing – review & editing, Writing – original draft, Visualization, Validation, Software, Resources, Methodology, Investigation, Formal analysis, Data curation. **Bagila Baitimbetova:** Writing – review & editing, Writing – original draft, Visualization, Validation, Software, Resources, Methodology, Investigation, Formal analysis, Data curation. **Philippe M. Heynderickx:** Writing – review & editing, Writing – original draft, Visualization, Validation, Software, Resources, Methodology, Investigation, Funding acquisition, Formal analysis, Data curation. **Ki-Hyun Kim:** Writing – review & editing, Writing – original draft, Visualization, Validation, Supervision, Software, Resources, Project administration, Methodology, Investigation, Funding acquisition, Formal analysis, Data curation. **Eilhann E. Kwon:** Writing – review & editing, Writing – original draft, Visualization, Validation, Resources, Methodology, Investigation, Formal analysis, Data curation.

Declaration of generative AI and AI-assisted technologies in the writing process

During the preparation of this work, the authors used AI-assisted technologies to improve language and readability. Specifically, ChatGPT (OpenAI) and Google's Large Language Model were utilized for grammar correction, sentence restructuring, and style enhancement. The authors reviewed and edited all AI-generated text to ensure accuracy and appropriateness for the scientific context. The authors take full responsibility for all content of the publication, including any remaining errors and the final scientific interpretations presented.

Declaration of competing interest

The authors declare that they have no known competing financial interests or personal relationships that could have appeared to influence the work reported in this paper.

Acknowledgments

This work was supported by a grant from the National Research Foundation of Korea (NRF) funded by the Ministry of Science and ICT (MSIT) of the Korean government (Grant Number: 2021R1A3B1068304)and by the CLEAN-AIR (Comprehensive Low Emission & Advanced Monitoring Network for Air Improvement & Renewal) R & D Program under grant number RS-2026-25504540. This work is financially supported by VinUniversity under Grant Number VINUNI.2526.CMIT.02. P.M.H. would like to thank the Research and Development Program of Ghent University Global Campus (GUGC), Korea.

Appendix A. Supplementary data

Supplementary data to this article can be found online at https://doi.org/10.1016/j.jsamd.2026.101279.

References

[1] V. Paranthaman, S. Lenus, L. Gnanasekaran, S. Kumaravel, M. Kumar, D. Shanmugapriya, M.F. Mohd Salleh, M.F. Mohd Sabri, Z. Dai, Defect-driven

material design for high-performance semiconducting gas sensing applications, J. Sci. Adv. Mater. Devices 11 (2026) 101150, https://doi.org/10.1016/j.jsamd.2026.101150.
[2] C. He, J. Cheng, X. Zhang, M. Douthwaite, S. Pattisson, Z. Hao, Recent advances in the catalytic oxidation of volatile organic compounds: a review based on pollutant sorts and sources, Chem. Rev. 119 (2019) 4471–4568, https://doi.org/10.1021/acs.chemrev.8b00408.
[3] Z. Xiao, X. Yang, H. Gu, J. Hu, T. Zhang, J. Chen, X. Pan, G. Xiu, W. Zhang, M. Lin, Characterization and sources of volatile organic compounds (VOCs) during 2022 summer ozone pollution control in Shanghai, China, Atmos. Environ. 327 (2024) 120464, https://doi.org/10.1016/j.atmosenv.2024.120464.
[4] Q. Yuan, Z. Zhang, M. Wang, K.F. Ho, T. Wang, S. Lee, Characterization of a smog chamber for studying formation of gas-phase products and secondary organic aerosol, J. Environ. Sci. 136 (2024) 570–582, https://doi.org/10.1016/j.jes.2022.12.027.
[5] J.S. Yang, W.Y. Jung, G.D. Lee, S.S. Park, E.D. Jeong, H.G. Kim, S.-S. Hong, Catalytic combustion of benzene over metal oxides supported on SBA-15, J. Ind. Eng. Chem. 14 (2008) 779–784, https://doi.org/10.1016/j.jiec.2008.05.008.
[6] H. Cheng, J. Hu, D. Wu, W. Bao, C. Hou, X. Lv, L. Chang, J. Wang, Effect of interaction between Pt and different crystalline phases of TiO_2 on benzene oxidation, Catalysts 14 (2024) 234, https://doi.org/10.3390/catal14040234.
[7] J. Wu, J. Tian, W. Zhou, S. Liu, D. Sun, SO_2-resistant hollow carbon spheres encapsulated Pt nanoparticles for benzene oxidation, Chem. Eng. J. 489 (2024) 151472, https://doi.org/10.1016/j.cej.2024.151472.
[8] J. Cui, Y. Cui, J. Tan, H. Zhang, M. Gu, L. Huang, Efficient catalytic oxidation of VOCs by a Pd-Pt/SiO_2 catalyst: the cooperative catalysis of dual metal sites, J. Environ. Chem. Eng. 12 (2024) 111930, https://doi.org/10.1016/j.jece.2024.111930.
[9] Q. Li, C. Deng, W. Zhou, P. Huang, C. Lu, H. Feng, L. Dong, L. Tan, Y.-W. Zhang, C. Zhou, Y. Qin, D. Xia, Ultrathin La_yCoO_x nanosheets with high porosity featuring boosted catalytic oxidation of benzene: mechanism elucidation via an experiment–theory combined paradigm, Inorg. Chem. 63 (2024) 3974–3985, https://doi.org/10.1021/acs.inorgchem.3c04621.
[10] H. Zhao, J. Wang, Engineering metal oxide catalyst for volatile organic compounds oxidation, Ionics 30 (2024) 11–25, https://doi.org/10.1007/s11581-023-05283-6.
[11] K. MohammedSaleh Katubi, N. Shaheen, S. Zulfiqar, A. Irshad, Z.A. Alrowaili, M. S. Al-Buriahi, I. Shakir, M.F. Warsi, E.W. Cochran, Innovative nanocomposites for enhanced photocatalytic removal of hazardous pollutants: probing the role of CuO/Fe_2O_3 and MXene synergy, Ind. Eng. Chem. Res. 63 (2024) 11922–11938, https://doi.org/10.1021/acs.iecr.4c00918.
[12] K. Muthusamy, P. Rameshkumar, L. Gnanasekaran, V. Paranthaman, D. Shanmugapriya, F. Arith, M. Aminul Islam, Neem-derived silver-decorated RGO/ZnO heterostructure nanocomposite: a bifunctional material for sunlight-driven photocatalysis and solar energy conversion, J. Sci. Adv. Mater. Devices 11 (2026) 101117, https://doi.org/10.1016/j.jsamd.2026.101117.
[13] N.E. Nfor, M.S. Khan, R. Sarwar, M. Bilal, A. Khan, S. Tasqeeruddin, M.F. Javed, N. Riaz, Ag/TiO_2-functionalized photocatalytic concrete for visible-light photocatalytic degradation of reactive black 5: experimental optimization, mechanistic insights and machine learning modeling, J. Sci. Adv. Mater. Devices 11 (2026) 101170, https://doi.org/10.1016/j.jsamd.2026.101170.
[14] M. Michalska, J. Pavlovsky, M. Sarman, K. Lemański, M. Mazurkiewicz-Pawlicka, A. Małolepszy, V. Novak, Y.-J. Chiou, P.B. Nagy, T. Szabo, Thermal modulation of Melem/g-C_3N_4 composites: structural evolution, optical tuning, and enhanced photocatalytic degradation of organic dyes, J. Sci. Adv. Mater. Devices 11 (2026) 101167, https://doi.org/10.1016/j.jsamd.2026.101167.
[15] J.H. Lee, H. Jang, J.-H. Kim, J.H. Park, K.-Y. Lee, M.B. Park, S.B. Kang, T.-S. Chang, I. Heo, Low temperature benzene oxidation over copper–silver catalyst: roles of copper oxide and silver on cerium–zirconium mixed oxide, Catal. Sci. Technol. 10 (2020) 6780–6789, https://doi.org/10.1039/D0CY00691B.
[16] K. Vikrant, K.-H. Kim, F. Dong, P.M. Heynderickx, D.W. Boukhvalov, Low-temperature oxidative removal of gaseous formaldehyde by an eggshell waste supported silver-manganese dioxide bimetallic catalyst with ultralow noble metal content, J. Hazard. Mater. 434 (2022) 128857, https://doi.org/10.1016/j.jhazmat.2022.128857.
[17] J.S. Yang, W.Y. Jung, G.-D. Lee, S.S. Park, S.-S. Hong, Effect of pretreatment conditions on the catalytic activity of benzene combustion over SBA-15-Supported copper oxides, Top. Catal. 53 (2010) 543–549, https://doi.org/10.1007/s11244-010-9484-x.
[18] P. Munnik, P.E. De Jongh, K.P. De Jong, Recent developments in the synthesis of supported catalysts, Chem. Rev. 115 (2015) 6687–6718, https://doi.org/10.1021/cr500486u.
[19] S.-H. Ha, J. Szulejko, K.-H. Kim, The feasibility and temporal storability of gas phase standards of volatile organic compounds prepared through liquid phase vaporization in polyester aluminum bags at room temperature, Chemosphere 291 (2022) 132965, https://doi.org/10.1016/j.chemosphere.2021.132965.
[20] S. Verma, K. Vikrant, K.-H. Kim, Optimization of process variables for the concurrent removal of aliphatic and aromatic volatile organic compounds over a copper impregnated titanium dioxide photocatalyst, Environ. Sci. Nano 10 (2023) 2035–2052, https://doi.org/10.1039/D3EN00178D.
[21] W.-K. Kim, K. Vikrant, S.A. Younis, K.-H. Kim, P.M. Heynderickx, Metal oxide/activated carbon composites for the reactive adsorption and catalytic oxidation of formaldehyde and toluene in air, J. Clean. Prod. 387 (2023) 135925, https://doi.org/10.1016/j.jclepro.2023.135925.
[22] Z. Jiang, C. He, N.F. Dummer, J. Shi, M. Tian, C. Ma, Z. Hao, S.H. Taylor, M. Ma, Z. Shen, Insight into the efficient oxidation of methyl-ethyl-ketone over hierarchically micro-mesostructured Pt/K-(Al)SiO_2 nanorod catalysts: structure-activity relationships and mechanism, Appl. Catal. B Environ. 226 (2018) 220–233, https://doi.org/10.1016/j.apcatb.2017.12.007.
[23] J.A. Onrubia-Calvo, A. Quindimil, A. Davó-Quiñonero, A. Bermejo-López, E. Bailón-García, B. Pereda-Ayo, D. Lozano-Castelló, J.A. González-Marcos, A. Bueno-López, J.R. González-Velasco, Kinetics, model discrimination, and parameters estimation of CO_2 methanation on highly active Ni/CeO_2 catalyst, Ind. Eng. Chem. Res. 61 (2022) 10419–10435, https://doi.org/10.1021/acs.iecr.2c00164.
[24] P. Malet, A. Caballero, The selection of experimental conditions in temperature-programmed reduction experiments, J. Chem. Soc. Faraday Trans. 1 Phys. Chem. Condens. Phases 84 (1988) 2369, https://doi.org/10.1039/f19888402369.
[25] J.M. Soler, E. Artacho, J.D. Gale, A. García, J. Junquera, P. Ordejón, D. Sánchez-Portal, The SIESTA method for ab initio order-N materials simulation, J. Phys. Condens. Matter 14 (2002) 2745–2779, https://doi.org/10.1088/0953-8984/14/11/302.
[26] M. Dion, H. Rydberg, E. Schröder, D.C. Langreth, B.I. Lundqvist, Van der Waals Density Functional for General Geometries, Phys. Rev. Lett. 92 (2004) 246401, https://doi.org/10.1103/PhysRevLett.92.246401.
[27] H. Rydberg, M. Dion, N. Jacobson, E. Schröder, P. Hyldgaard, S.I. Simak, D. C. Langreth, B.I. Lundqvist, Van der Waals Density Functional for Layered Structures, Phys. Rev. Lett. 91 (2003) 126402, https://doi.org/10.1103/PhysRevLett.91.126402.
[28] J.P. Perdew, K. Burke, M. Ernzerhof, Generalized gradient approximation made simple, Phys. Rev. Lett. 78 (1997), https://doi.org/10.1103/PhysRevLett.78.1396, 1396–1396.
[29] N. Troullier, J.L. Martins, Efficient pseudopotentials for plane-wave calculations, Phys. Rev. B 43 (1991) 1993–2006, https://doi.org/10.1103/PhysRevB.43.1993.
[30] J.-M. Kim, K. Vikrant, T. Kim, K.-H. Kim, F. Dong, Thermocatalytic oxidation of gaseous benzene by a titanium dioxide supported platinum catalyst, Chem. Eng. J. 428 (2022) 131090, https://doi.org/10.1016/j.cej.2021.131090.
[31] M. Shaban, J. Poostforooshan, A.P. Weber, Surface-initiated polymerization on unmodified inorganic semiconductor nanoparticles via surfactant-free aerosol-based synthesis toward core–shell nanohybrids with a tunable shell thickness, J. Mater. Chem. A 5 (2017) 18651–18663, https://doi.org/10.1039/C7TA04985D.
[32] X. Li, C. Wang, J. Yang, Y. Xu, Y. Yang, J. Yu, J.J. Delgado, N. Martsinovich, X. Sun, X.-S. Zheng, W. Huang, J. Tang, PdCu nanoalloy decorated photocatalysts for efficient and selective oxidative coupling of methane in flow reactors, Nat. Commun. 14 (2023) 6343, https://doi.org/10.1038/s41467-023-41996-y.
[33] M. Thommes, K. Kaneko, A.V. Neimark, J.P. Olivier, F. Rodriguez-Reinoso, J. Rouquerol, K.S.W. Sing, Physisorption of gases, with special reference to the evaluation of surface area and pore size distribution (IUPAC technical report), Pure Appl. Chem. 87 (2015) 1051–1069, https://doi.org/10.1515/pac-2014-1117.
[34] A.F. Zedan, S. Gaber, A.S. AlJaber, K. Polychronopoulou, CO oxidation at near-ambient temperatures over TiO_2-Supported Pd-Cu catalysts: promoting effect of Pd-Cu nanointerface and TiO_2 morphology, Nanomaterials 11 (2021) 1675, https://doi.org/10.3390/nano11071675.
[35] P. Kitsiou, N. Lagopati, E.-P. Tsilibary, P. Falaras, P. Papazafiri, E.P. Pavlatou, E. Kotsopoulou, Effect of nanostructured TiO_2 crystal phase on photoinduced apoptosis of breast cancer epithelial cells, Int. J. Nanomed. (2014) 3219, https://doi.org/10.2147/IJN.S62972.
[36] J. Jiang, X.X. Liu, J. Han, K. Hu, J.S. Chen, Self-supported sheets-on-wire CuO@Ni$(OH)_2$/$Zn(OH)_2$ nanoarrays for high-performance flexible quasi-solid-state supercapacitor, Processes 9 (2021) 680, https://doi.org/10.3390/pr9040680.
[37] C. Liu, X. Guo, Z.-F. Huang, J. Li, L. Gan, L. Pan, C. Shi, X. Zhang, G. Yang, J.-J. Zou, Surface defect-regulated PdCu/TiO_{2-x} promoting efficient electrocatalytic nitrogen reduction, Mater. Chem. Front. 6 (2022) 2190–2200, https://doi.org/10.1039/D2QM00453D.
[38] Q. Wei, Q. Ma, P. Zuo, H. Fan, S. Qu, W. Shen, Hollow structure and electron promotion effect of mesoporous Pd/CeO_2 catalyst for enhanced catalytic hydrogenation, ChemCatChem 10 (2018) 1019–1026, https://doi.org/10.1002/cctc.201701457.
[39] F. Platero, A. López-Martín, A. Caballero, T.C. Rojas, M. Nolan, G. Colón, Overcoming Pd–TiO_2 deactivation during H_2 production from photoreforming using Cu@Pd nanoparticles supported on TiO_2, ACS Appl. Nano Mater. 4 (2021) 3204–3219, https://doi.org/10.1021/acsanm.1c00345.
[40] R. Monjezi, A. Bouriakova, A. Bjelić, P.M. Heynderickx, G.J. Heynderickx, D. Poelman, J.-M. Giraudon, J.-F. Lamonier, R. Morent, J.W. Thybaut, Mechanistic insights into methane total oxidation over Cu/Hydroxyapatite catalyst synthesized with β-Cyclodextrin assistance, Chem. Eng. J. 489 (2024) 151324, https://doi.org/10.1016/j.cej.2024.151324.
[41] M.P. Heynderickx, J.W. Thybaut, H. Poelman, D. Poelman, G.B. Marin, Kinetic modeling of the total oxidation of propane over CuO-CeO_2/γ-Al_2O_3, Appl. Catal. B Environ. 95 (2010) 26–38, https://doi.org/10.1016/j.apcatb.2009.11.018.
[42] X. Wang, W. Zhao, X. Wu, T. Zhang, Y. Liu, K. Zhang, Y. Xiao, L. Jiang, Total oxidation of benzene over ACo_2O_4 (A = Cu, Ni and Mn) catalysts: in situ DRIFTS account for understanding the reaction mechanism, Appl. Surf. Sci. 426 (2017) 1198–1205, https://doi.org/10.1016/j.apsusc.2017.07.269.
[43] K. Vikrant, K.-H. Kim, D.W. Boukhvalov, P.M. Heynderickx, Benzene oxidation in air by an amine-functionalized metal–organic framework-derived Carbon- and nitrogen-loaded zirconium dioxide-supported platinum catalyst, ACS Appl. Mater. Interfaces 16 (2024) 33669–33687, https://doi.org/10.1021/acsami.4c07188.
[44] I. Triandafillidi, M.G. Kokotou, D. Lotter, C. Sparr, C.G. Kokotos, Aldehyde-catalyzed epoxidation of unactivated alkenes with aqueous hydrogen peroxide, Chem. Sci. 12 (2021) 10191–10196, https://doi.org/10.1039/D1SC02360H.

[45] X.-P. Yu, D. Wang, D.-X. Tian, Z.-Y. Tian, Revisit the benzene oxidation at elevated pressure, Combust. Flame 265 (2024) 113469, https://doi.org/10.1016/j.combustflame.2024.113469.
[46] M. Döntgen, K. Leonhard, Reactions of chemically activated formic acid formed via HĊO + ȮH, J. Phys. Chem. A 120 (2016) 1819–1824, https://doi.org/10.1021/acs.jpca.6b00887.
[47] M. Kawasaki, T. Ibuki, M. Iwasaki, Y. Takezaki, Vacuum-ultraviolet photolysis of ethylene oxide, J. Chem. Phys. 59 (1973) 2076–2082, https://doi.org/10.1063/1.1680294.
[48] J. Lee, J.W. Bozzelli, Thermochemical and kinetic analysis of the Formyl methyl radical + O_2 reaction system, J. Phys. Chem. A 107 (2003) 3778–3791, https://doi.org/10.1021/jp030001o.
[49] D. Srivastava, W. Li, S. Tong, Z. Shi, R.M. Harrison, Characterization of products formed from the oxidation of toluene and m-xylene with varying NO_x and OH exposure, Chemosphere 334 (2023) 139002, https://doi.org/10.1016/j.chemosphere.2023.139002.
[50] J.F. Stevens, C.S. Maier, Acrolein: sources, metabolism, and biomolecular interactions relevant to human health and disease, Mol. Nutr. Food Res. 52 (2008) 7–25, https://doi.org/10.1002/mnfr.200700412.
[51] J.F. Lockyear, O. Welz, J.D. Savee, F. Goulay, A.J. Trevitt, C.A. Taatjes, D. L. Osborn, S.R. Leone, Isomer specific product detection in the reaction of CH with Acrolein, J. Phys. Chem. A 117 (2013) 11013–11026, https://doi.org/10.1021/jp407428v.
[52] S. Pakhira, R.I. Singh, O. Olatunji-Ojo, M. Frenklach, W.A. Lester, Quantum Monte Carlo study of the reactions of CH with Acrolein: major and minor channels, J. Phys. Chem. A 120 (2016) 3602–3612, https://doi.org/10.1021/acs.jpca.5b11527.
[53] S. Haq, R.C. Bainbridge, B.G. Frederick, N.V. Richardson, Anhydride ring chemistry at a metal surface, J. Phys. Chem. B 102 (1998) 8807–8815, https://doi.org/10.1021/jp9822283.
[54] N. Montoya Sánchez, A. De Klerk, Autoxidation of aromatics, Appl. Petrochem. Res. 8 (2018) 55–78, https://doi.org/10.1007/s13203-018-0199-4.
[55] H.R. Bizzo, N.S. Brilhante, Y. Nolvachai, P.J. Marriott, Use and abuse of retention indices in gas chromatography, J. Chromatogr. A 1708 (2023) 464376, https://doi.org/10.1016/j.chroma.2023.464376.
[56] M.B. Wilson, B.B. Barnes, P.G. Boswell, What experimental factors influence the accuracy of retention projections in gas chromatography–mass spectrometry? J. Chromatogr. A 1373 (2014) 179–189, https://doi.org/10.1016/j.chroma.2014.11.030.
[57] H. Cao, X. Li, Y. Chen, M. Gong, J. Wang, Effect of loading content of copper oxides on performance of Mn-Cu mixed oxide catalysts for catalytic combustion of benzene, J. Rare Earths 30 (2012) 871–877, https://doi.org/10.1016/S1002-0721(12)60148-3.
[58] W. Tang, X. Wu, S. Li, X. Shan, G. Liu, Y. Chen, Co-nanocasting synthesis of mesoporous Cu–Mn composite oxides and their promoted catalytic activities for gaseous benzene removal, Appl. Catal. B Environ. 162 (2015) 110–121, https://doi.org/10.1016/j.apcatb.2014.06.030.
[59] D. Li, Y. Fan, Y. Ding, X. Wei, Y. Xiao, Preparation of cobalt-copper-aluminum spinel mixed oxides from layered double hydroxides for total oxidation of benzene, Catal. Commun. 88 (2017) 60–63, https://doi.org/10.1016/j.catcom.2016.09.035.